Computerized Medical Imaging and Graphics 100 (2022) 102071

Contents lists available at ScienceDirect

Computerized Medical Imaging and Graphics

journal homepage: www.elsevier.com/locate/compmedimag

Model-based super-resolution reconstruction with joint motion estimation for improved quantitative MRI parameter mapping

Quinten Beirinckx [a,d,*,1], Ben Jeurissen [a,d], Michele Nicastro [a,d], Dirk H.J. Poot [b], Marleen Verhoye [c,d], Arnold J. den Dekker [a,d], Jan Sijbers [a,d]

[a] imec-Vision Lab, Department of Physics, University of Antwerp, Antwerp, Belgium
[b] Biomedical Imaging Group Rotterdam, Department of Radiology and Nuclear Medicine, Erasmus MC, Rotterdam, The Netherlands
[c] Bio-Imaging Lab, Department of Biomedical Sciences, University of Antwerp, Antwerp, Belgium
[d] μNEURO Research Centre of Excellence, University of Antwerp, Antwerp, Belgium

ARTICLE INFO

Keywords:
Bayesian estimation
Model-based reconstruction
Motion correction
Quantitative magnetic resonance imaging
Super-resolution

ABSTRACT

Quantitative Magnetic Resonance (MR) imaging provides reproducible measurements of biophysical parameters, and has become an essential tool in clinical MR studies. Unfortunately, 3D isotropic high resolution (HR) parameter mapping is hardly feasible in clinical practice due to prohibitively long acquisition times. Moreover, accurate and precise estimation of quantitative parameters is complicated by inevitable subject motion, the risk of which increases with scanning time. In this paper, we present a model-based super-resolution reconstruction (SRR) method that jointly estimates HR quantitative parameter maps and inter-image motion parameters from a set of 2D multi-slice contrast-weighted images with a low through-plane resolution. The method uses a Bayesian approach, which allows to optimally exploit prior knowledge of the tissue and noise statistics. To demonstrate its potential, the proposed SRR method is evaluated for a T1 and T2 quantitative mapping protocol. Furthermore, the method's performance in terms of precision, accuracy, and spatial resolution is evaluated using simulated as well as real brain imaging experiments. Results show that our proposed fully flexible, quantitative SRR framework with integrated motion estimation outperforms state-of-the-art SRR methods for quantitative MRI.

1. Introduction

In recent decades, magnetic resonance imaging (MRI) has evolved from a qualitative imaging tool to a quantitative measurement method. Whereas qualitative MRI relies on the subjective interpretation of tissue contrast, quantitative MRI (qMRI) aims to measure reproducible and objective maps of biophysical parameters, which allows the comparison of measurements across subjects and sites, or over time (*e.g.*, longitudinal follow-up of patients). Indeed, biophysical parameters measured by qMRI, such as relaxation times and diffusion metrics, are increasingly used as biomarkers for neurological diseases (Seiler et al., 2021), in quantitative musculoskeletal imaging (de Mello et al., 2019), or in qMRI-guided radiotherapy (van Houdt et al., 2021). Unfortunately, despite its broad range of potential applications, qMRI is not widely used in clinical practice. This is mainly because qMRI requires a series of MR images with different contrast weightings to estimate the biophysical parameter maps of interest and suffers from long scan times to provide accurate and precise parameter maps at 3D isotropic high spatial resolution. Methods have been proposed that enable reconstruction from highly under-sampled images and hence speed up image acquisition, such as model-based reconstruction (Maier et al., 2019), low-rank approaches (Zhang et al., 2015), or the imposition of sparsity constraints (Zhao et al., 2012). However, they generally come at the cost of either a lower precision or a lower spatial resolution of the reconstructed parameter maps.

To break the trade-off between resolution, precision and acquisition time, super-resolution reconstruction (SRR) has been put forward (Greenspan et al., 2002; Van Reeth et al., 2012). In this approach, high-resolution (HR) 3D isotropic images are estimated from a set of multi-slice images with a high in-plane but low through-plane resolution, where the multi-slice images are acquired with either sub-voxels shifts in the through-plane direction (Greenspan et al., 2002), three orthogonal slice orientations (Rousseau et al., 2006; Gholipour et al., 2010; Scherrer et al., 2012; Sui et al., 2021), slice orientations rotated

* Correspondence to: Vision Lab, University of Antwerp (CDE), Universiteitsplein 1, N.1.16, B-2610 Antwerpen, Belgium.
E-mail address: quinten.beirinckx@uantwerpen.be (Q. Beirinckx).
[1] [orcid=0000-0002-5339-052X]

https://doi.org/10.1016/j.compmedimag.2022.102071
Received 26 November 2021; Received in revised form 7 April 2022; Accepted 29 April 2022
Available online 10 May 2022

around a common frequency encoding axis (Shilling et al., 2009), or arbitrary slice orientations (Poot et al., 2010b). SRR has indeed been shown to provide a better trade-off between acquisition time, spatial resolution, and signal-to-noise ratio (SNR) than conventional direct HR acquisition (Plenge et al., 2012). Meanwhile, SRR has also been successfully applied to different qMRI modalities, including diffusion MRI (Poot et al., 2013; Fogtmann et al., 2014; Van Steenkiste et al., 2016), relaxometry (Van Steenkiste et al., 2017; Bano et al., 2020; Lajous et al., 2020) and arterial spin labeling (Bladt et al., 2020). In some of these approaches, HR images are individually reconstructed from a set of equally contrast-weighted LR images, prior to voxel-wise fitting a parametric qMRI signal model (*e.g.*, a diffusion model or relaxation model) to these reconstructed HR images (Poot et al., 2013; Lajous et al., 2020), whereas in other approaches the qMRI signal model is included in the reconstruction and HR parameter maps are estimated directly from the LR images, without first reconstructing the individual HR contrast-weighted images (Fogtmann et al., 2014; Van Steenkiste et al., 2016, 2017; Bano et al., 2020).

In addition to the challenge of 3D isotropic HR parameter mapping, the long qMRI scan times come with an increased risk of patient motion. If this motion is not properly accounted for, the spatial resolution of the obtained parameter maps will be negatively affected. Like conventional qMRI methods, SRR methods for qMRI usually correct for motion by performing image registration as a pre-processing step, prior to the estimation of the HR parameter maps (Van Steenkiste et al., 2016, 2017), where the latter step is often preceded by an intermediate step of HR image reconstruction (Scherrer et al., 2012; Poot et al., 2013). A downside to this multi-step approach is the lack of a feedback mechanism that connects the motion compensation routine with the final estimation of the HR parameter maps. As a result, registration errors may propagate into the parameter estimation step, introducing a bias (Nachmani et al., 2019).

To avoid error propagation, image registration can be integrated in a joint motion/qMRI parameter estimation framework. This strategy has already been successfully applied to correct inter-scan motion in T_1 mapping (Ramos-Llordén et al., 2017) or to correct for motion in multi-shell diffusion MRI (Christiaens et al., 2021). At the same time, methods have been proposed that combine SRR with joint motion estimation for anatomical (qualitative) MRI (Rousseau et al., 2006, 2010; Jiang et al., 2007; Gholipour et al., 2010; Fogtmann et al., 2012; Kainz et al., 2015; Ebner et al., 2020). However, until now, the development of a unified motion estimation/SRR approach for qMRI has received little attention (Fogtmann et al., 2014; Beirinckx et al., 2020).

In the present work, we propose a multi-frame model-based SRR method for multi-parametric quantitative MRI with integrated inter-image motion estimation in a Bayesian Maximum a Posteriori (MAP) estimation framework. As a guiding application, we focus on MR relaxometry, but the method's modular construction ensures an easy adaption to other qMRI modalities. The novelty of the method lies in its unique combination of properties that makes it stand out from existing SRR methods in qMRI. First, by combining super-resolution image reconstruction and quantitative parameter estimation in a single integrated model-based approach, 3D HR biophysical parameter maps are estimated directly from a set of multi-slice differently contrast-weighted LR images, which distinguishes our method from two-step qMRI SRR approaches that reconstruct individual HR images from equally contrast-weighted LR images prior to voxel-wise fitting a qMRI signal model (*e.g.* a relaxation model or diffusion model) to these reconstructed images (Poot et al., 2013; Lajous et al., 2020). Second, the joint estimation of the motion and the biophysical parameters of interest allows our method to outperform state-of-the-art qMRI SRR algorithms that either do not correct for motion (Bano et al., 2020), or work with decoupled motion estimation algorithms (Van Steenkiste et al., 2017). Third, unlike state-of-the-art SRR methods in qMRI that rely on orthogonal slice orientations and use the same set of contrast weightings for each slice orientation (*e.g.*, Fogtmann et al., 2014), our method allows for arbitrary slice orientations and a different contrast weighting for each LR image, offering a much-increased imaging flexibility. Finally, its Bayesian estimation approach allows our method to optimally exploit prior knowledge of tissue properties and noise statistics, as opposed to standard regularized least-squares methods (Poot et al., 2010b; Van Steenkiste et al., 2017; Bano et al., 2020; Lajous et al., 2020).

To demonstrate its potential, the proposed unified quantitative SRR method is evaluated for T_1 mapping and T_2 mapping. Its performance in terms of accuracy, precision and mean squared error is extensively validated using synthetic whole brain simulations. Finally, the applicability of the SRR method is demonstrated on *in-vivo* brain data and its performance on brain structure delineation (spatial resolution) is evaluated.[2]

2. Theory

This section introduces the forward model of the SRR problem considered in this work. It describes the relation between the LR images and the HR parameter maps to be reconstructed and accounts for unintended motion. Furthermore, the Bayesian Maximum a Posteriori (MAP) estimator is introduced that is used to estimate the HR maps jointly with the motion parameters, accounting for the MR data distribution and using a total variation (TV) prior for the HR maps and a non-informative prior for the motion parameters.

2.1. Forward model

Let $\boldsymbol{s} = \{\boldsymbol{s}_n\}_{n=1}^{N}$ be the set of N vectorized noiseless anisotropic LR multi-slice contrast-weighted magnitude images, where $\boldsymbol{s}_n = \{s_{nl}\}_{l=1}^{N_s} \in \mathbb{R}^{N_s \times 1}$ is sampled at the LR grid points $\boldsymbol{y}_n = \{\boldsymbol{y}_{nl}\}_{l=1}^{N_s} \in \mathbb{R}^{3 \times N_s}$ with N_s the number of voxels per LR image. Then, each $\boldsymbol{s}_n$ can be modelled as:

$$\boldsymbol{s}_n = |\boldsymbol{D}\boldsymbol{B}\boldsymbol{G}_n\boldsymbol{M}_{\boldsymbol{\theta}_n}\boldsymbol{r}_n|, \tag{1}$$

where $|\cdot|$ denotes the pointwise modulus operator and $\boldsymbol{r}_n = \{\boldsymbol{r}_{nj}\}_{j=1}^{N_r} \in \mathbb{R}^{N_r \times 1}$ represents the virtual, noise-free HR image assumed to be acquired with the same contrast-weighting settings as $\boldsymbol{s}_n$ and defined at the targeted isotropic HR grid points $\boldsymbol{x} = \{\boldsymbol{x}_j\}_{j=1}^{N_r} \in \mathbb{R}^{3 \times N_r}$, with N_r the number of voxels of the HR image. Furthermore, $\boldsymbol{M}_{\boldsymbol{\theta}_n} \in \mathbb{R}^{N_r \times N_r}$, $\boldsymbol{G}_n \in \mathbb{R}^{N_r \times N_r}$, $\boldsymbol{B} \in \mathbb{R}^{N_r \times N_r}$, and $\boldsymbol{D} \in \mathbb{R}^{N_s \times N_r}$ are linear operators that describe motion, a known geometric transformation that maps the grid coordinates of the HR image $\boldsymbol{r}_n$ to those of the LR image $\boldsymbol{s}_n$, spatially invariant blurring, and down-sampling, respectively. The motion operator $\boldsymbol{M}_{\boldsymbol{\theta}_n}$ is modeled as a parametric function of $\boldsymbol{\theta}_n$. Assuming rigid inter-image motion, the parameter vector $\boldsymbol{\theta}_n \in \mathbb{R}^{6 \times 1}$ is given by

$$\boldsymbol{\theta}_n = \left[t_{xn}, t_{yn}, t_{zn}, \alpha_n, \beta_n, \gamma_n\right]^T, \tag{2}$$

with t_{xn}, t_{yn}, t_{zn} the translation parameters and α_n, β_n, γ_n the Euler angles of three elementary rotation matrices that describe rotation around the x, y and z axis, respectively. The operator $\boldsymbol{G}_n$ models the SRR acquisition scheme. In the SRR acquisition scheme considered in this work, the LR images each have a different slice orientation, where the different orientations are obtained by rotating around a fixed encoding axis. Detailed descriptions of the warping operator $\boldsymbol{M}_{\boldsymbol{\theta}_n}$, which is analytically differentiable w.r.t. $\boldsymbol{\theta}_n$, as well as the operators $\boldsymbol{G}_n$, $\boldsymbol{B}$, and $\boldsymbol{D}$ are included as part of the supplementary material.

In qMRI, one is not so much interested in the voxel intensities of the HR images $\boldsymbol{r}_n$, but rather in the values of the underlying biophysical

[2] A preliminary study of our framework, implementing a maximum likelihood instead of a Bayesian approach and covering a limited number of simulation results, was published as a proceedings paper (Beirinckx et al., 2020).

tissue parameters in those voxels, such as the proton densities and T_1 and T_2 relaxation times. Let $\boldsymbol{\vartheta} = \{\boldsymbol{\vartheta}_q\}_{q=1}^{Q} \in \mathbb{R}^{N_r \times Q}$ be the biophysical parameter maps to be inferred, with $\boldsymbol{\vartheta}_q = \{\vartheta_{qj}\}_{j=1}^{N_r} \in \mathbb{R}^{N_r \times 1}$ the q^{th} tissue parameter map and $\boldsymbol{\vartheta}_{\bullet j} \in \mathbb{R}^{Q \times 1}$ all tissue parameters of the j^{th} voxel of $\boldsymbol{\vartheta}_q$. Then, the j^{th} voxel of the HR image $\boldsymbol{r}_n$, can be modelled as

$$r_{nj} = f_n(\boldsymbol{\vartheta}_{\bullet j}) \tag{3}$$

with $f_n(\boldsymbol{\vartheta}_{\bullet j}) : \mathbb{R}^{Q \times 1} \mapsto \mathbb{R}$ a relaxometry, diffusion, or perfusion model, or any other qMRI model that describes the relation between r_{nj} and the underlying biophysical tissue parameters $\boldsymbol{\vartheta}_{\bullet j}$ in the corresponding voxel. In the current work, the proposed SRR method is evaluated for T_1 and T_2 relaxometry, using the signal models described in section 3. The forward model of the SRR reconstruction problem considered in this work is obtained by substituting Eq. (3) in Eq. (1). The parameters to be estimated are the parameter maps $\boldsymbol{\vartheta}$ and motion parameters $\boldsymbol{\theta} = \{\boldsymbol{\theta}_n\}_{n=1}^{N}$.

2.2. Joint Bayesian estimation framework

2.2.1. Bayes theorem

Let $\widetilde{\boldsymbol{s}} = \{\widetilde{\boldsymbol{s}}_n\}_{n=1}^{N} \in \mathbb{R}^{N_s \times N}$ denote the set of N measured LR multi-slice images with $\widetilde{\boldsymbol{s}}_n = \{\widetilde{s}_{nl}\} \in \mathbb{R}^{N_s \times 1}$. Following a Bayesian approach, both the data $\widetilde{\boldsymbol{s}}$ and the parameters $\{\boldsymbol{\vartheta}, \boldsymbol{\theta}\}$ to be estimated are modeled as random variables, where Bayes' theorem gives an expression for the *posterior* distribution of the parameters given the data:

$$p(\boldsymbol{\vartheta}, \boldsymbol{\theta} | \widetilde{\boldsymbol{s}}) = \frac{p(\widetilde{\boldsymbol{s}} | \boldsymbol{\vartheta}, \boldsymbol{\theta}) p(\boldsymbol{\vartheta}) p(\boldsymbol{\theta})}{p(\widetilde{\boldsymbol{s}})} \quad , \tag{4}$$

with $p(\widetilde{\boldsymbol{s}} | \boldsymbol{\vartheta}, \boldsymbol{\theta})$ the *likelihood* function of the data, $p(\boldsymbol{\vartheta})$ and $p(\boldsymbol{\theta})$ the *prior* distributions that encapsulate the prior knowledge about $\boldsymbol{\vartheta}$ and $\boldsymbol{\theta}$, respectively, and $p(\widetilde{\boldsymbol{s}})$ a scaling factor that can be ignored since it does not affect the estimator that will be described below.

2.2.2. Maximum a posteriori estimator

The MAP estimator maximizes $p(\boldsymbol{\vartheta}, \boldsymbol{\theta} | \widetilde{\boldsymbol{s}})$ w.r.t. the parameters $\{\boldsymbol{\vartheta}, \boldsymbol{\theta}\}$:

$$\{\widehat{\boldsymbol{\vartheta}}, \widehat{\boldsymbol{\theta}}\} = \underset{\boldsymbol{\vartheta}, \boldsymbol{\theta}}{\operatorname{argmax}}\, p(\boldsymbol{\vartheta}, \boldsymbol{\theta} | \widetilde{\boldsymbol{s}}). \tag{5}$$

Eq. (5) is typically solved by minimizing the negative logarithm of $p(\boldsymbol{\vartheta}, \boldsymbol{\theta} | \widetilde{\boldsymbol{s}})$.

2.2.3. Likelihood function

Without loss of generalization, the measured LR images $\widetilde{\boldsymbol{s}}$ are assumed to be Rician distributed, which is a valid noise model for magnitude images reconstructed from single-coil k-space data (den Dekker and Sijbers, 2014), for images reconstructed from multi-coil data with SENSE (Aja-Fernández et al., 2014), or with GRAPPA jointly with a spatial-matched-filter or the Adaptive Combine method (Walsh et al., 2000). Then, the probability density function (PDF) of $\widetilde{s}_{nl}$ is given by:

$$p(\widetilde{s}_{nl} | \boldsymbol{\vartheta}, \boldsymbol{\theta}_n) = \frac{\widetilde{s}_{nl}}{\sigma_{nl}^2} e^{-\frac{\widetilde{s}_{nl}^2 + s_{nl}^2(\boldsymbol{\vartheta}, \boldsymbol{\theta}_n)}{2\sigma_{nl}^2}} I_0\left(\frac{\widetilde{s}_{nl} s_{nl}(\boldsymbol{\vartheta}, \boldsymbol{\theta}_n)}{\sigma_{nl}^2}\right) u(\widetilde{s}_{nl}), \tag{6}$$

with $I_0(\cdot)$ the zeroth order modified Bessel function of the first kind, and σ_{nl} the non-stationary (*i.e.* spatially-dependent) standard deviation of the Gaussian noise disturbing the complex data underlying the magnitude MR data. The unit step function $u(\cdot)$ is used to indicate that (6) is non-zero for non-negative values of $\widetilde{s}_{nl}$ only. Assuming all voxels to be statistically independent, the joint PDF of $\widetilde{\boldsymbol{s}}$ is given by

$$p(\widetilde{\boldsymbol{s}} | \boldsymbol{\vartheta}, \boldsymbol{\theta}) = \prod_{n=1}^{N} \prod_{l=1}^{N_s} p(\widetilde{s}_{nl} | \boldsymbol{\vartheta}, \boldsymbol{\theta}_n). \tag{7}$$

When (7) is viewed as a function of the unknown parameters $\{\boldsymbol{\vartheta}, \boldsymbol{\theta}\}$ given the data $\widetilde{\boldsymbol{s}}$, it is called the *likelihood* function. It follows from (6) and (7) that the negative log-likelihood function $\mathscr{L}_{\widetilde{\boldsymbol{s}}} \equiv -\log p(\widetilde{\boldsymbol{s}} | \boldsymbol{\vartheta}, \boldsymbol{\theta})$ can be written as (Sijbers et al., 1998)

$$\mathscr{L}_{\widetilde{\boldsymbol{s}}}(\boldsymbol{\vartheta}, \boldsymbol{\theta} | \widetilde{\boldsymbol{s}}) = \sum_{n=1}^{N} \sum_{l=1}^{N_s} \Bigg[-\log \widetilde{s}_{nl} + \log \sigma_{nl}^2 + \frac{\widetilde{s}_{nl}^2}{2\sigma_{nl}^2} + \frac{s_{nl}^2(\boldsymbol{\vartheta}, \boldsymbol{\theta}_n)}{2\sigma_{nl}^2} - \log I_0\left(\frac{\widetilde{s}_{nl} s_{nl}(\boldsymbol{\vartheta}, \boldsymbol{\theta}_n)}{\sigma_{nl}^2}\right) \Bigg]. \tag{8}$$

Furthermore, it is assumed that the noise standard deviations can be estimated prior to the construction of the MAP estimator of $\{\boldsymbol{\vartheta}, \boldsymbol{\theta}\}$ using tailored noise estimation routines (Aja-Fernández et al., 2015; Pieciak et al., 2017; Maitra and Faden, 2009; Bouhrara et al., 2017).

2.2.4. Prior distributions

For each of the Q HR tissue parameter maps associated with $\boldsymbol{\vartheta}$, a discretized upwind TV prior (Chambolle et al., 2011) is chosen as:

$$p(\boldsymbol{\vartheta}_q) \propto \exp\{-\frac{2}{\lambda_q} \mathrm{TV}(\boldsymbol{\vartheta}_q)\}, \quad \text{with} \quad q = 1, \ldots, Q, \tag{9}$$

where $\lambda_q > 0$ denotes the hyperparameter to be selected by the user, as will be discussed in section 2.2.6, and with

$$\mathrm{TV}(\boldsymbol{\vartheta}_q) = \sum_j \left[\sqrt{\begin{matrix} \epsilon^2 & +(\Delta^{x,+}(\vartheta_{qj}))^2 + (\Delta^{x,-}(\vartheta_{qj}))^2 \\ & +(\Delta^{y,+}(\vartheta_{qj}))^2 + (\Delta^{y,-}(\vartheta_{qj}))^2 \\ & +(\Delta^{z,+}(\vartheta_{qj}))^2 + (\Delta^{z,-}(\vartheta_{qj}))^2 \end{matrix}} - \epsilon \right], \tag{10}$$

where $\Delta^{x,+}(\vartheta_{qj})$, $\Delta^{x,-}(\vartheta_{qj})$, $\Delta^{y,+}(\vartheta_{qj})$, $\Delta^{y,-}(\vartheta_{qj})$, $\Delta^{z,+}(\vartheta_{qj})$, and $\Delta^{z,-}(\vartheta_{qj})$ represent the forward (+) and backward (−) first order differences, in the x-, y-, and z-direction, at the j^{th} HR voxel of the parameter map $\boldsymbol{\vartheta}_q$. Furthermore, a small value $\epsilon > 0$ is introduced, to avoid derivative singularities of TV when $\boldsymbol{\vartheta}_q$ is locally constant.

For the motion parameters $\boldsymbol{\theta}$, a non-informative prior $p(\boldsymbol{\theta})$ is adopted, assuming $p(\boldsymbol{\theta})$ to be uniform over the range of values for which the likelihood function is non-negligible.

2.2.5. Alternating minimization

The nonlinear optimization problem (5) is solved using the *alternating minimization* method, also known as the cyclic block-coordinate descent (cBCD) method (Fessler and Kim, 2011; Beck and Tetruashvili, 2013). In this method, the parameters $\{\boldsymbol{\vartheta}, \boldsymbol{\theta}\}$ are split into two blocks that contain the motion parameters $\boldsymbol{\theta}$ and the tissue parameters $\boldsymbol{\vartheta}$, respectively, and the cost function is successively minimized with respect to each block in a cyclic order:

$$\widehat{\boldsymbol{\theta}}^{(t+1)} = \underset{\boldsymbol{\theta}}{\operatorname{argmin}}\, \mathscr{L}_{\widetilde{\boldsymbol{s}}}(\widehat{\boldsymbol{\vartheta}}^{(t)}, \boldsymbol{\theta} | \widetilde{\boldsymbol{s}}) \tag{P.1}$$

$$\widehat{\boldsymbol{\vartheta}}^{(t+1)} = \underset{\boldsymbol{\vartheta}}{\operatorname{argmin}} \left[\mathscr{L}_{\widetilde{\boldsymbol{s}}}(\boldsymbol{\vartheta}, \widehat{\boldsymbol{\theta}}^{(t+1)} | \widetilde{\boldsymbol{s}}) + \sum_{q=1}^{Q} \frac{2}{\lambda_q} \mathrm{TV}(\boldsymbol{\vartheta}_q) \right] \tag{P.2}$$

with $\widehat{\boldsymbol{\vartheta}}^{(0)} = \boldsymbol{\vartheta}_{\text{ini}}$, and $\widehat{\boldsymbol{\theta}}^{(0)} = \boldsymbol{\theta}_{\text{ini}}$ the initial values of the HR tissue parameters $\boldsymbol{\vartheta}$ and the motion parameters $\boldsymbol{\theta}$, respectively. The procedure is terminated when a maximum number of iterations, $t_{\max}$, is exceeded, or when a convergence tolerance on the relative difference of the tissue parameter estimates between consecutive iterations is reached. The pseudo-code of our proposed MAP estimation framework is presented in Algorithm 1. The initial values $\boldsymbol{\vartheta}_{\text{ini}}$, and $\boldsymbol{\theta}_{\text{ini}}$ are obtained using a *while*-loop routine consisting of three main steps. First, a HR magnitude contrast-weighted image is approximated from each LR contrast-weighted image by applying the adjoint operator $\boldsymbol{M}_{\boldsymbol{\theta}_n}^T \boldsymbol{G}_n^T \boldsymbol{B}^T \boldsymbol{D}^T$ of the SRR forward model (1) to each LR image, followed by the application of the pointwise modulus operator $|\cdot|$, to regain magnitude images. Second, initial tissue parameter values $\boldsymbol{\vartheta}_{\text{ini}}$ are obtained by voxel-wise nonlinear least-squares (NLLS) fitting the modulus of the signal model

(12) to these upsampled LR images with a Levenberg-Marquardt algorithm. In a third step, problem (P.1) is solved to obtain initial estimates for the motion parameters $\boldsymbol{\theta}_{\text{ini}}$, where the tissue parameter estimates of the second step are kept fixed in the cost function $\mathscr{L}_{\tilde{s}}(\widehat{\boldsymbol{\vartheta}}^{(t+1)}, \widehat{\boldsymbol{\theta}}|\tilde{s})$.

The *inter-image* motion estimation problem (P.1) adopts a particularly simple structure when the signal model parameters remain fixed. If no dependence of $\{\boldsymbol{\theta}_n\}_{n=1}^{N}$ through index n is assumed, the minimization can be decoupled into N optimization problems, which can be implemented very efficiently by parallel operations. Each of these decoupled problems is minimized using a trust-region Newton algorithm (Coleman and Li, 1994), with analytical expressions for the Jacobian to speed up convergence. The derivation of these expressions is included as part of the supplementary material provided with this paper. To solve the large-scale optimization problem (P.2), a trust-region-reflective Newton algorithm is used (Coleman and Li, 1994), with analytical expressions for the Jacobian and Hessian, which have also been included as part of the supplementary material.

Algorithm 1. (*Model-based SRR with joint motion estimation (SRR-joint)*)

Input: LR images $\tilde{s}$ and initial values $\boldsymbol{\vartheta}_{\text{ini}}$ and $\boldsymbol{\theta}_{\text{ini}}$
Output: MAP estimates $\widehat{\boldsymbol{\vartheta}}_{\text{MAP}}$ and $\widehat{\boldsymbol{\theta}}_{\text{MAP}}$
Set $t \leftarrow 0$ and $\widehat{\boldsymbol{\vartheta}}^{(0)}, \widehat{\boldsymbol{\theta}}^{(0)} \leftarrow \boldsymbol{\vartheta}_{\text{ini}}, \boldsymbol{\theta}_{\text{ini}}$;
$\mathscr{E}^{(0)} = \varkappa \mathscr{E}_{\min}$, with $\varkappa \in \mathbb{R}_{>1}$;
while $\mathscr{E}^{(t)} \geq \mathscr{E}_{\min}$ and $t < t_{\max}$ **do**
  |▷ Solve (P.1) to get $\widehat{\boldsymbol{\theta}}^{(t+1)}$:
  | $\widehat{\boldsymbol{\theta}}^{(t+1)} = \underset{\boldsymbol{\theta}}{\text{argmin}}\, \mathscr{L}_{\tilde{s}}(\widehat{\boldsymbol{\vartheta}}^{(t)}, \boldsymbol{\theta}|\tilde{s})$, started from $\boldsymbol{\theta} \leftarrow \widehat{\boldsymbol{\theta}}^{(t)}$;
  |▷ Solve (P.2) to get $\widehat{\boldsymbol{\vartheta}}^{(t+1)}$:
  | $\widehat{\boldsymbol{\vartheta}}^{(t+1)} = \underset{\boldsymbol{\vartheta}}{\text{argmin}} \left[\mathscr{L}_{\tilde{s}}(\boldsymbol{\vartheta}, \widehat{\boldsymbol{\theta}}^{(t+1)}|\tilde{s}) + \sum_{q=1}^{Q} \frac{2}{\lambda_q} \text{TV}(\boldsymbol{\vartheta}_q) \right]$, started from $\boldsymbol{\vartheta} \leftarrow \widehat{\boldsymbol{\vartheta}}^{(t)}$;
  |▷ Calculate[a] $\mathscr{E}^{(t+1)} = \| \widehat{\boldsymbol{\vartheta}}^{(t+1)} - \widehat{\boldsymbol{\vartheta}}^{(t)} \|_2 / \| \widehat{\boldsymbol{\vartheta}}^{(t+1)} \|_2$;
  |▷ Set $t \leftarrow t + 1$;
end
$\widehat{\boldsymbol{\vartheta}}_{\text{MAP}} = \widehat{\boldsymbol{\vartheta}}^{(t)}$ and $\widehat{\boldsymbol{\theta}}_{\text{MAP}} = \widehat{\boldsymbol{\theta}}^{(t)}$;
return $\widehat{\boldsymbol{\vartheta}}_{\text{MAP}}, \widehat{\boldsymbol{\theta}}_{\text{MAP}}$;

[a] Vectorization of SRR $\widehat{\boldsymbol{\vartheta}}^{(t+1)}$ and $\widehat{\boldsymbol{\vartheta}}^{(t)}$ is performed before taking the norm.

2.2.6. Regularization parameter selection

The hyperparameters $\lambda_1, \ldots, \lambda_Q$ of the prior distribution (9) act as regularization parameters that balance data consistency (as quantified by the likelihood function) against the requirement that the parameter maps be smooth (as imposed by the TV prior). The selection of the regularization parameters of a nonlinear optimization problem like the one at hand is a challenging task for which no standard procedure exists. Poorly chosen regularization parameters may lead to either over-smoothing or under-smoothing. In this work, the individual regularization parameters were determined such that the corresponding TV terms contribute equally to the cost function of (P.2). To this end, each TV term of (P.2) is evaluated in the initial estimates of the respective tissue parameter map, and the ratio of each TV value to the TV value of the first tissue parameter is used to determine the regularization parameters $\lambda_2, \ldots, \lambda_Q$ as a function of λ_1. More specifically, this leads to $\lambda_q = \left[\text{TV}(\widehat{\boldsymbol{\vartheta}}_{q,\text{ini}})/\text{TV}(\widehat{\boldsymbol{\vartheta}}_{1,\text{ini}})\right] \cdot \lambda_1$. As such, the multi-parameter regularization selection problem is cast into a single-parameter regularization problem. The remaining regularization parameter, λ_1, is chosen empirically.

3. Materials and methods

The proposed model-based Bayesian SRR method with joint motion estimation was validated in whole brain simulations choosing T_1 relaxometry as a showcase example. Next, to demonstrate the ability of the proposed method to improve the quality of reconstructed parameter maps, a proof-of-concept evaluation was performed for a T_1 and T_2 quantitative mapping protocol using two contrast-weighted *in vivo* brain datasets.

The following parametric signal models were adopted in this work:

- T_1 *relaxation* signal model of the gold standard inversion recovery (IR) sequence (Barral et al., 2010):

$$f_n(\boldsymbol{\vartheta}_{\bullet j}) = \rho_j \left(1 - (1 - \cos\alpha) e^{-\frac{\text{TI}_n}{T_{1,j}}} + e^{-\frac{\text{TR}}{T_{1,j}}}\right), \tag{11}$$

  with TI_n the n^{th} inversion time, α the inversion pulse angle, TR the repetition time and $\boldsymbol{\vartheta}_{\bullet j} = [\rho_j, T_{1,j}]^T$ the tissue parameter vector at position $\boldsymbol{x}_j$, in which ρ_j is a parameter proportional to the proton density and receiver gain and $T_{1,j}$ is the longitudinal relaxation time. Assuming $\alpha = 180^\circ$ and $\text{TR} \gg T_1$, Eq. (11) simplifies to

$$f_n(\boldsymbol{\vartheta}_{\bullet j}) = \rho_j \left(1 - 2\, e^{-\frac{\text{TI}_n}{T_{1,j}}}\right). \tag{12}$$

- T_2 *relaxation* signal model of a conventional Multiple-Echo Spin Echo (MESE) sequence (Carr and Purcell, 1954):

$$f_n(\boldsymbol{\vartheta}_{\bullet j}) = \rho_j e^{-\frac{\text{TE}_n}{T_{2,j}}}, \tag{13}$$

  with TE_n the n^{th} echo time, and $\boldsymbol{\vartheta}_{\bullet j} = [\rho_j, T_{2,j}]^T$ the tissue parameter vector at position $\boldsymbol{x}_j$, in which ρ_j is again a parameter proportional to the proton density and receiver gain and $T_{2,j}$ is the transverse relaxation time. Note that we have assumed a perfect 90° excitation pulse to tilt the magnetization vector in the transverse plane, and perfect 180° refocusing pulses to recover multiple spin echoes corresponding with T_2 estimates along the signal envelope.

The proposed SRR method was compared with an SRR approach without motion estimation, and one in which SRR is preceded by a motion compensation step. To sum up, the following three frameworks were compared against each other:

1. **SRR-static**: a model-based SRR framework without motion estimation. This approach consists of three steps. First, a HR magnitude image is approximated from each LR image using the adjoint operator $\boldsymbol{G}_n^T \boldsymbol{B}^T \boldsymbol{D}^T$ of the SRR forward model (1), followed by application of the pointwise modulus operator $|\cdot|$. Second, voxel-wise NLLS fitting of the modulus of the signal model is performed using a Levenberg-Marquardt algorithm to obtain initial parameter map estimates. Finally, problem (P.2) is solved assuming $\widehat{\boldsymbol{\theta}} = \boldsymbol{0}$.
2. **SRR-reg**: a model-based SRR framework in which the inter-image motion parameters are estimated prior to the SRR by means of an advanced registration routine (Van Steenkiste et al., 2017). In this approach, a registration routine is performed consisting of four steps, where the first two steps correspond with the first two steps of SRR-static. In a third step, LR images are simulated using the estimated HR parameter maps from the previous step and the forward model (1). As a fourth step, rigid motion parameter estimates $\boldsymbol{\theta}_{\text{REG}}$ are obtained from pairwise rigid registration using a mean squared error metric and a regular step gradient descent optimization algorithm (MaxIter = 800, GradientMagnitudeTolerance = 10^{-12}). In order to obtain rigid motion parameters that can be used as input parameters of the motion operator $\boldsymbol{M}_{\boldsymbol{\theta}n}$, which is part of the forward model in problem (P.2), registration needs to be performed on the HR grid. As such, the simulated and acquired LR image datasets to be co-registered are transformed to the HR grid using the adjoint operator $\boldsymbol{G}_n^T \boldsymbol{B}^T \boldsymbol{D}^T$ of the SRR forward model (1). Next, steps 1-4 are repeated until a convergence tolerance $\mathscr{E}_{\min} = 10^{-4}$ on the relative difference of the tissue parameter estimates between consecutive iterations is met. Finally, problem (P.2) is solved in which motion

parameter estimates $\boldsymbol{\theta}_{\text{REG}}$ obtained from the registration routine remain fixed.

3. **SRR-joint**: the proposed SRR framework with joint motion estimation, as described in section 2.2. The pseudo code of this framework is described in Algorithm 1. The maximum number of iterations and the tolerance criterion to halt the algorithm were chosen to be $t_{\max} = 80$ and $\mathscr{E}_{\min} = 10^{-4}$, respectively.

For the *in vivo* experiments described in subsection 3.2, the regularization parameters of SRR-joint were chosen following the procedure described in subsection 2.2.6, yielding $2/\lambda_1 = 1.1 \times 10^{-2}$ and $2/\lambda_2 = 5.6 \times 10^{-3}$ for the *in vivo* T_1 mapping experiment, and $2/\lambda_1 = 2.4 \times 10^{-2}$ and $2/\lambda_2 = 1.0 \times 10^{-2}$ for the *in vivo* T_2 mapping experiment, respectively. Next, the same regularization parameters were used for SRR-static and SRR-reg, to guarantee a fair comparison. Finally, the same regularization weights as for the *in vivo* T_1 mapping experiment were also used for the whole brain Monte Carlo simulation experiments described in the next subsection.

3.1. Whole brain simulations

Ground truth $\boldsymbol{T}_1$ and $\boldsymbol{\rho}$ parameter maps for a synthetic whole brain Monte Carlo simulation experiment were generated from parameter maps obtained after model-based SRR on the T_1-weighted *in vivo* dataset, further described in section 3.2. Both HR parameter maps were of size $160 \times 160 \times 160$, with an isotropic voxel size of 1.6 mm.

From these ground truth parameter maps, $N_{\text{MC}} = 8$ Rician distributed realisations of a LR T_1-weighted dataset were simulated. Each dataset consisted of $N = 14$ images with $\log(\text{TI}_n)$ equidistant between $\log(100\,\text{ms})$ and $\log(3000\,\text{ms})$ (Van Steenkiste et al., 2017). The LR images were synthesized using the forward model (1), with an image size of $160 \times 160 \times 40$ and with an anisotropic voxel size of $1.6 \times 1.6 \times 6.4\,\text{mm}^3$. The inter-image motion parameters $\{\boldsymbol{\theta}_n\}_{n=1}^{N}$ were chosen equal to an estimated set of motion parameters obtained from model-based SRR with SRR-joint on the T_1-weighted *in vivo* dataset to guarantee realistic head movement. The extreme and mean values for each of the motion parameters are reported in Table S1 of the supplementary file.

Similar to the acquisition protocol used in (Van Steenkiste et al., 2016, 2017) and the acquisition protocol in the *in vivo* experiments (cfr. subsection 3.2), the LR images were simulated with different slice orientations, where the rotation was performed around the phase encoding axis in increments of $180/N_0$ degrees, with $N_0 = 7$ the number of slice orientations. Since rotation in image space corresponds to rotation in frequency domain, this acquisition scheme ensures that each LR image covers a different part of the *k*-space (as shown in the top row of Fig. 1) (Plenge et al., 2012). Two LR images were simulated for each slice orientation, where each of the thus resulting $N = 14$ images had a unique inversion time. An overview of the slice orientations and inversion times of the T_1-weighted LR images, along with their *k*-space coverage, is given in Fig. 1.

Finally, the LR T_1-weighted images were corrupted with spatially variant Rician noise, where the spatially variant noise pattern corresponded with an isotropic Gaussian function to model the gradual deterioration of the head coil detection towards the center of the brain (Pieciak et al., 2017). The level of the noise map was adjusted to match that of the *in vivo* T_1-weighted dataset that will be described in the next subsection. To this end, the overall SNR, defined as the ratio of the

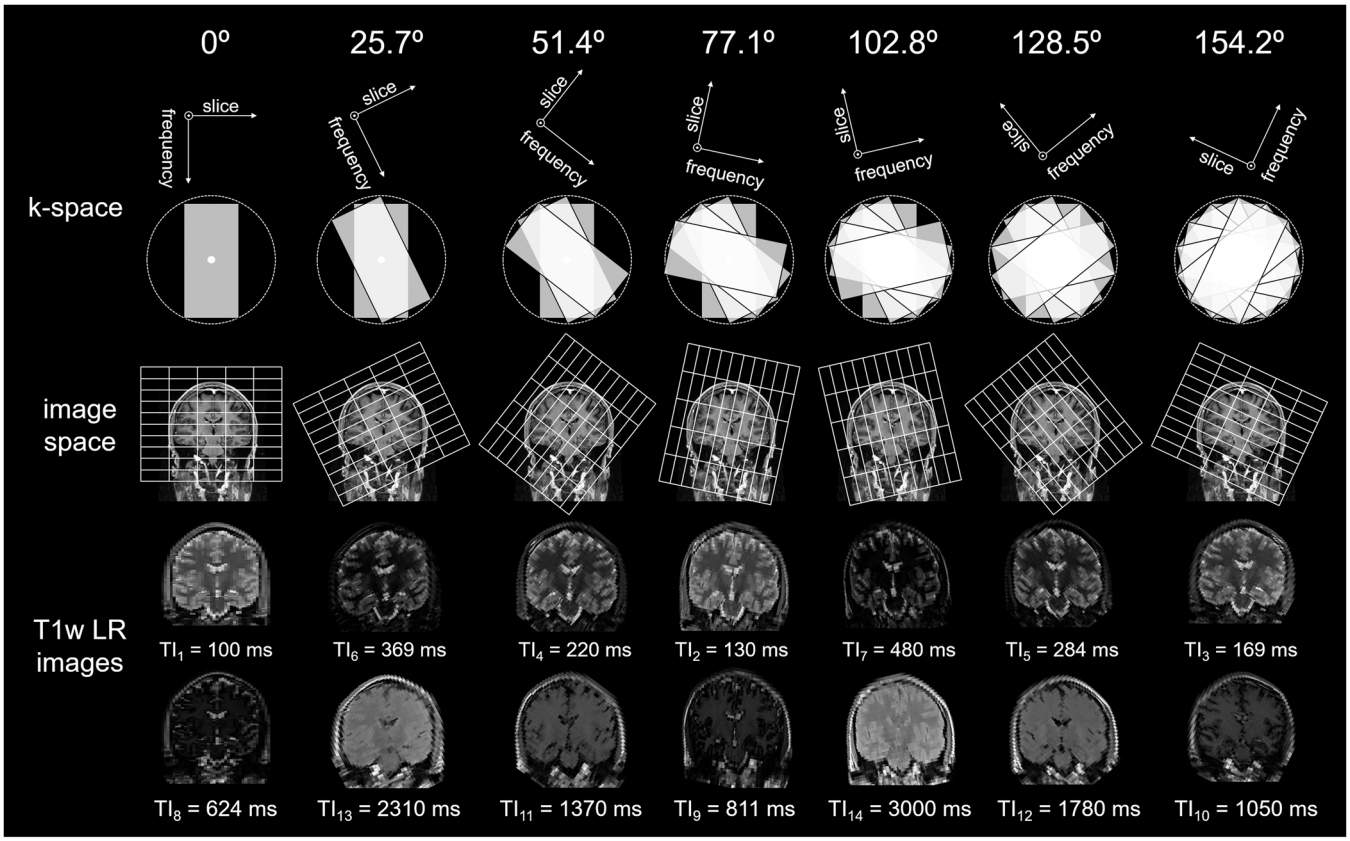

Fig. 1. Overview of the different slice orientations for the LR T_1-weighted *in vivo* (and simulated) dataset(s), together with a schematic representation of the overlap in *k*-space when images are combined. Fourteen 2D IR TSE T_1-weighted LR images were acquired with large slice thickness and a high in-plane resolution. The slice orientation was consecutively altered by rotation over a specified angle (0°, 25.7°, 51.4°, …, 154.2°) around the phase-encoding direction. As indicated, each T_1-weighted LR image was acquired with a unique inversion time.

spatial mean of the signal to the standard deviation of the noise, where the latter is estimated using the method of Coupé *et al.* (Coupé et al., 2010), was calculated in a small homogeneous region of the corpus callosum of the *in vivo* T_1-weighted image acquired with TI = 100 ms, and observed to be 16. Next, the level of the noise map of the simulated T_1-weighted images was adjusted to match this SNR value in the corpus callosum of the simulated image sampled at the same inversion time. In all simulation SRR experiments, the noise standard deviation maps were assumed to be known.

3.2. In vivo data

The proposed SRR method was validated using two *in vivo* human brain datasets suffering from involuntary patient motion. Both healthy volunteers (adult, male, 28 and 32 years old) were scanned after written informed consent and approval by the institutional ethics committee using a 3 T MRI scanner (Magnetom PrismaFit, Siemens Healthcare, Erlangen, Germany) with VE11B software, a maximum gradient amplitude of 80 mT/m, a maximum slew rate of 200 T/m/s, and a dedicated head-coil with 32 receiver channels. Magnitude data was reconstructed from the complex coil images using the adaptive combine algorithm (Walsh et al., 2000).

The first *in vivo* LR dataset consisted of a series of T_1-weighted LR images with anisotropic voxel size. In total, 14 repetitions of an interleaved multi-slice IR TSE with low through-plane resolution (voxel size, $1.0 \times 1.0 \times 4.0$ mm^3), with turbo factor 10, without slice gap, and with 100% sampling, were acquired. The slice thickness of the LR dataset was chosen to have whole brain coverage without exceeding SAR limits. The acquisition matrix was equal to 256×256, with a total number of slices equal to 40. Furthermore, the bandwidth was fixed at 305 Hz/pixel, and the TR and echo time (TE) were equal to 5000 ms and 8.8 ms, respectively. No in-plane acceleration was used. Each acquisition was characterized by a specific rotation around the phase-encoding axis and a unique inversion time, where the rotation angles and inversion times agree with those used in the simulation study, as summarized in Fig. 1. The scan time per anisotropic 2D slice stack was 2 min 3 s, resulting in a total scan time of 28 min 44 s. SRR was performed at an isotropic HR grid with a voxel size of $1.0 \times 1.0 \times 1.0$ mm^3. Spatially variant noise standard deviation maps were estimated using the method of (Aja-Fernández et al., 2015).

A second *in vivo* T_2-weighted anisotropic LR dataset was acquired, using 7 repetitions of an interleaved multislice MESE acquisition with low through-plane resolution (voxel size, $1.75 \times 1.75 \times 7.0$ mm^3), without slice gap, using a 3-fold in-plane GRAPPA acceleration factor with 24 reference lines. The acquisition matrix was equal to 128×128, with a total number of slices equal to 26. The bandwidth was fixed at 227 Hz/pixel. Each MESE acquisition was characterized by a unique rotation around the phase-encoding axis (rotations similar as in Fig. 1), and consisted of 4 unique echo times. An overview of the sampled TEs per MESE acquisition is given in Table 1. The echo time spacing ΔTE in each MESE was chosen as such to ensure full coverage of the T2 relaxation curve when all 7 acquisitions are combined. This is illustrated in more detail in Fig. S4 of the supplementary file. The TR = 4320 ms was kept constant for each MESE acquisition to avoid differences in T_1-weighting. In addition, the first echo of each MESE acquisition was ignored in the SRR reconstruction, which is a common consideration for MESE acquisitions (Petrovic et al., 2015), to avoid protruding errors from imperfect refocusing and stimulated (secondary) echoes that disrupt the T_2 decay of the primary SEs. In this way, the total count of sampled TEs was limited to 21. The scan time per anisotropic 2D MESE acquisition was 4 min 11 s, resulting in a total scan time for this proof-of-concept protocol of 29 min 17 s. SRR was performed at an isotropic HR grid with a voxel size of $1.75 \times 1.75 \times 1.75$ mm^3, and non-stationary noise standard deviation maps were again estimated using the method of (Aja-Fernández et al., 2015).

3.3. Quantitative image analysis

The results of the synthetic whole brain Monte Carlo simulation experiment were assessed quantitatively using the following performance measures (Ramos-Llordén et al., 2017; Beirinckx et al., 2020):

(a) *Relative bias*. The bias quantifies the *accuracy* of an estimator (van den Bos, 2007). Relative bias maps were calculated for each framework as $(\overline{\widehat{\boldsymbol{\vartheta}}}_q - \boldsymbol{\vartheta}_q) \oslash \boldsymbol{\vartheta}_q$, where $\overline{\widehat{\boldsymbol{\vartheta}}}_q$ and $\boldsymbol{\vartheta}_q$ refer to the tissue parameter maps which contain the element-wise sample mean of the N_{MC} estimates $\widehat{\boldsymbol{\vartheta}}_q$, and the true reference values, respectively, and where $\oslash$ denotes the element-wise division operator.

(b) *Relative standard deviation*. The standard deviation quantifies the *precision* of an estimator (van den Bos, 2007). Relative standard deviation maps were calculated for each framework as $\left(\frac{N_{\mathrm{MC}}}{N_{\mathrm{MC}}-1}\overline{(\widehat{\boldsymbol{\vartheta}}_q - \overline{\widehat{\boldsymbol{\vartheta}}}_q) \circ (\widehat{\boldsymbol{\vartheta}}_q - \overline{\widehat{\boldsymbol{\vartheta}}}_q)}\right)^{\circ\frac{1}{2}} \oslash \boldsymbol{\vartheta}_q$, where $\circ$ and the superscript $\circ\frac{1}{2}$ denote the Hadamard product and element-wise square-root operator, respectively.

(c) *Relative root-mean-squared error (relative RMSE)*. The RMSE is a measure that incorporates both accuracy and precision. Relative RMSE maps were calculated as $\left(\overline{(\widehat{\boldsymbol{\vartheta}}_q - \boldsymbol{\vartheta}_q) \circ (\widehat{\boldsymbol{\vartheta}}_q - \boldsymbol{\vartheta}_q)}\right)^{\circ\frac{1}{2}} \oslash \boldsymbol{\vartheta}_q$.

Additionally, the spatial means of the relative bias, standard deviation and RMSE maps were calculated inside a brain mask, which was extracted from the reference ρ map using the Brain Extraction Tool (BET) (Smith, 2002).

To assess the ability of the different frameworks to estimate motion, the following performance measure was used:

(a) *Motion component root-(mean)-mean-squared-error (RMMSE)*, defined as

Table 1
Distribution of echo times per MESE acquisition for the *in vivo* T_2 mapping experiment. Slice orientation angles corresponds with those given in Fig. 1. The first echo times that were ignored to alleviate the effect of stimulated secondary echoes are highlighted in bold.

	Slice orient. angle [°]	$\mathbf{TE_1}$	TE_2	TE_3	TE_4
MESE 1	0	**10.0**	20.0	30.0	40.0
MESE 2	25.7	**11.8**	23.6	35.4	47.2
MESE 3	51.4	**19.2**	38.4	57.6	76.8
MESE 4	77.1	**22.6**	45.2	67.8	90.4
MESE 5	102.8	**34.0**	68.0	102.0	136.0
MESE 6	128.5	**36.9**	73.8	110.7	147.6
MESE 7	154.2	**40.0**	80.0	120.0	160.0

$$\left(\frac{1}{N}\sum_{n=1}^{N}\overline{(\widehat{\boldsymbol{\theta}}_n-\boldsymbol{\theta}_n)\circ(\widehat{\boldsymbol{\theta}}_n-\boldsymbol{\theta}_n)}\right)^{\circ\frac{1}{2}}, \tag{14}$$

where $\boldsymbol{\theta}_n$ refers to the true reference values and the operator $\overline{(\cdot)}$ denotes the element-wise sample mean over the N_{MC} estimates $\widehat{\boldsymbol{\theta}}_n$.

For the *in vivo* T_1 mapping experiment, results were quantitatively assessed in terms of spatial resolution and SNR efficiency. Spatial resolution of the obtained parameter maps was assessed in all 3 image dimensions by measuring the average width over 15 edge profiles. The sample of edge profiles was selected in one parameter map (cfr. Fig. S3 of the supplementary file), and then consistently compared across all the parameter maps of the respective frameworks. The edge width, defined as the width (in high resolution voxels) from 10% to 90% of the edge height, was measured by least squares fitting with a sigmoid function:

$$\eta(x) = a_1 + \frac{a_2}{1+\exp(-a_3(x-a_4))}, \tag{15}$$

from which the edge width can be derived, given by $4.4/a_3$ (Greenspan et al., 2002).

Furthermore, SNR measurements were obtained from the *in vivo* reconstruction results for each framework. First, volumes-of-interest (VOIs) were manually delineated in uniform regions of white matter, CSF, and the caudate nucleus of the ρ map reconstructed with the SRR-joint framework. For the aforementioned tissue types, the VOIs had volumes equal to 100 mm^3, 21 mm^3, and 48 mm^3, respectively. Next, the same VOIs were selected in the T_1 map reconstructed with SRR-joint, and in the ρ and T_1 maps reconstructed with SRR-static and SRR-reg. Subsequently, the SNR was calculated in each VOI as the ratio of the spatial mean to the standard deviation.

3.4. Implementation

All algorithms were written in MATLAB and partially in C++, and run on a computer with an Intel® Core™ i7–6850 K hexa-core CPU with 15 MB of cache clocked at 3.60 GHz, with 32 GB of RAM. The computational complexity of the proposed SRR-joint algorithm is primarily defined by the Fast Fourier Transform (FFT)-based image warping operators $\boldsymbol{M}_{\boldsymbol{\theta}_n}$ and $\boldsymbol{G}_n$ in the forward model (1). The FFT-based implementation allows to solve the inverse SRR problem using exact adjoint image warping, and avoids inaccuracies caused by an approximate inverse of the motion. To speed up reconstruction, the FFTs of both image warping operators are executed on the GPU, reducing reconstruction time by a factor of 2–6 compared to pure MATLAB code, mainly dependent on the number of LR images and corresponding image dimensions. In addition, as mentioned in section 2.2.5, MATLAB parallel computing tools were used to estimate $\boldsymbol{\theta}_n$ for each value of n separately when solving problem (P.2) of the alternating minimization method. Similarly, voxel-wise NLLS model fitting during the initialization step of the different SRR frameworks was performed in a parallel manner. Also, to avoid excessive memory usage, the Hessian matrix of problem (P.2) was implemented using a Hessian multiply function, which gives the result of a Hessian-times-vector product without computing the Hessian directly. A more extensive description of the computational requirements, with additional implementation details, is given in section 2 of the supplementary file.

4. Results

4.1. Whole brain simulations

Table 2 summarizes the quantitative performance measures that were obtained from the whole brain simulation experiment for the frameworks SRR-static, SRR-reg, and SRR-joint. Corresponding standard errors and 95% confidence intervals for each value are included in Table S2 of the supplementary file. For each performance measure, the best performing framework is highlighted in bold. It follows from Table 2 that in terms of accuracy SRR-joint clearly outperforms SRR-static (with a factor 2) and SRR-reg. In terms of precision, SRR-static outperforms the other two approaches, as indicated by the lower overall standard deviation. However, in terms of the overall RMSE, SRR-joint performs best, both for T_1 and ρ mapping.

Table 2
Quantitative performance measures for the whole brain simulations, calculated over $N_{\mathrm{MC}} = 8$ reconstruction results, for each SRR framework.

	SRR-static	SRR-reg	SRR-joint
Overall rel. bias			
T_1 [%]	16.840	10.121	**8.698**
ρ [%]	64.530	30.875	**24.075**
Overall rel. std. dev.			
T_1 [%]	**0.316**	0.591	0.686
ρ [%]	**0.842**	1.072	1.313
Overall rel. RMSE			
T_1 [%]	16.855	10.176	**8.799**
ρ [%]	64.547	30.945	**24.204**
RMMSE			
t_x [mm]	0.374	0.095	**0.063**
t_y [mm]	1.381	0.321	**0.027**
t_z [mm]	1.543	0.285	**0.043**
α [degree]	1.207	0.346	**0.019**
β [degree]	0.245	0.111	**0.015**
γ [degree]	0.261	0.078	**0.008**

The absence of motion estimation in the SRR framework becomes evident by looking at maps of the relative RMSE (Fig. 2), for each of the three SRR frameworks. A closer look at these maps, shows the improved performance in terms of accuracy of the SRR-joint framework compared to the other two approaches. Here, the joint estimation of motion parameters allows for a more accurate estimation of tissue parameters at tissue interfaces, in particular for interfaces at tissue types with longer T_1 relaxation times such as the corpus callosum, and voxels at the periphery of the brain. Additionally, maps of the absolute value of the relative bias and of the relative standard deviation are included in Fig. S1 and Fig. S2 of the supplementary file.

4.2. In vivo data

Fig. 3 shows orthogonal mid-slice views of a directly acquired IR TSE T_1-weighted image with low through-plane resolution sampled at TI = 100 ms, and a synthesized T_1-weighted image with high through-plane resolution that was produced from the SRR T_1 and ρ parameter map estimates at the same TI. To ease qualitative comparison, zoomed image regions are shown indicating noticeable resolution improvements. The corresponding quantitative T_1 relaxation and ρ parameter map estimates that were obtained using the proposed SRR-joint framework are also shown in Fig. 3. The improved resolution in each orthogonal plane is clearly visible. In particular, SRR manages to recover the fine details lost due to the acquisition with low through-plane resolution.

Next, to compare the reconstruction results for the LR-T1w *in vivo* dataset, Fig. 4 shows the estimated T_1 and ρ parameter maps obtained using SRR-static, SRR-reg, and SRR-joint, respectively. Fig. 4 also shows the absolute value of the relative difference between the reconstructed parameter maps obtained with SRR-static and SRR-reg, taking the corresponding parameter maps obtained with the SRR-joint framework as a reference. Based on Fig. 4, it can be deduced that the joint estimation of motion parameters yields visible differences at the tissue interfaces, with a noticeably better delineation of the various brain structures. This is also confirmed by the edge width measurements for the T_1 and ρ

parameter maps summarized in Table 3, where SRR-joint achieves smaller edge widths, *i.e.* a higher spatial resolution, for all parameter maps as compared to SRR-static and SRR-reg. Furthermore, SNR measurements for the selected VOIs in the reconstructed tissue parameter maps of the *in vivo* data experiment were consistently higher for SRR-joint as compared to the other two frameworks, except for the SNR value of CSF in the ρ parameter map (Table 3). Standard errors and 95% confidence intervals for the edge width and SNR measurements are included in Table S3 of the supplementary file.

In addition, Fig. 5 shows a directly acquired IR TSE T_1-weighted image with low through-plane resolution compared to synthesized T_1-weighted images with high through-plane resolution, that were produced from the SRR T_1 and ρ parameter map estimates for each framework. Note that SRR-joint outperforms SRR-static and SRR-reg, showing enhanced delineation of brain structures, as indicated by the yellow arrows for different regions of interest.

The reconstruction results for the SRR-joint framework on the *in vivo* T_2-weighted dataset are summarized in Fig. 6. This figure shows orthogonal mid-slice views of a directly acquired MESE T_2-weighted image with low through-plane resolution sampled at TE = 42.7 ms, a synthesized T_2-weighted image with high through-plane resolution that was produced from the SRR T_2 and ρ parameter map estimates sampled

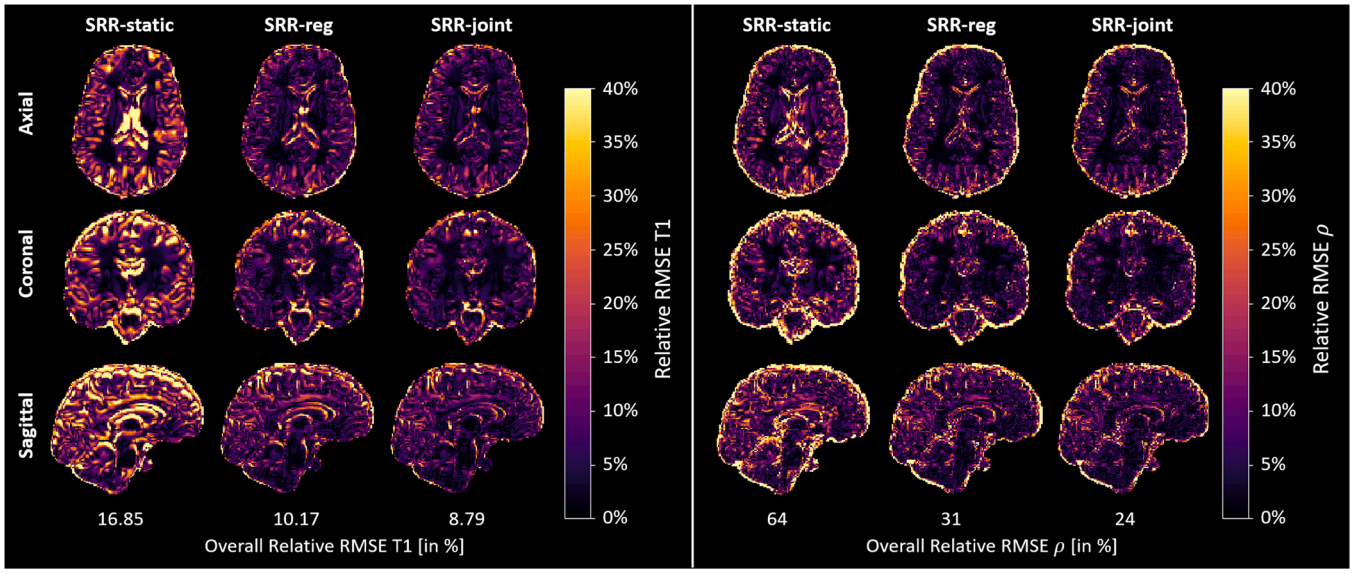

Fig. 2. Relative RMSE maps for T_1 and ρ, calculated from the reconstruction results of the synthetic whole brain simulations. For each of the different model-based SRR frameworks orthogonal mid-slice views are shown. Numbers at the bottom of the images indicate the overall relative RMSE measure, which was obtained by calculating the spatial mean of the corresponding relative RMSE map.

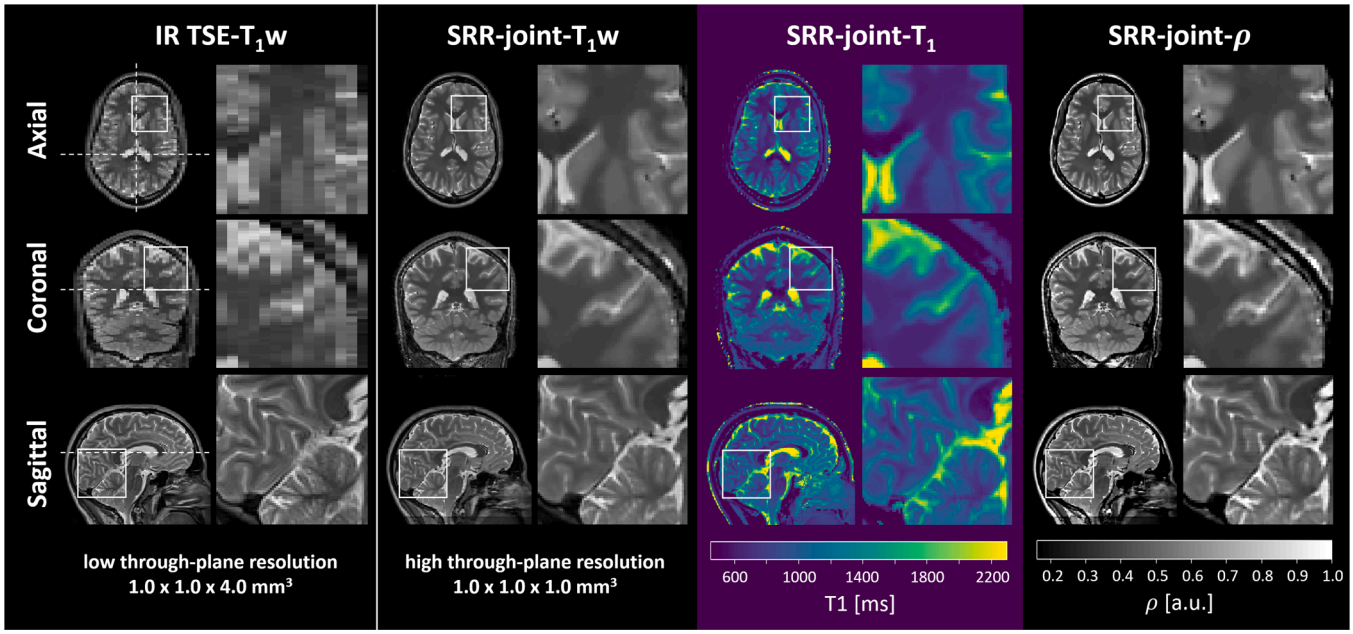

Fig. 3. Orthogonal mid-slice views with zoomed close-ups showing the resolution improvement for a directly acquired IR TSE T_1-weighted image with low through-plane resolution sampled at TI_1 (first column), compared to a synthesized T_1-weighted image with high through-plane resolution (second column), that was produced from the SRR T_1 and ρ parameter map estimates (columns 3 and 4) sampled at the same inversion time. Note that for the LR-T1w *in vivo* data set, SRR-joint can recover the fine details lost to the acquisition with low through-plane resolution. Dashed lines indicate the slice locations.

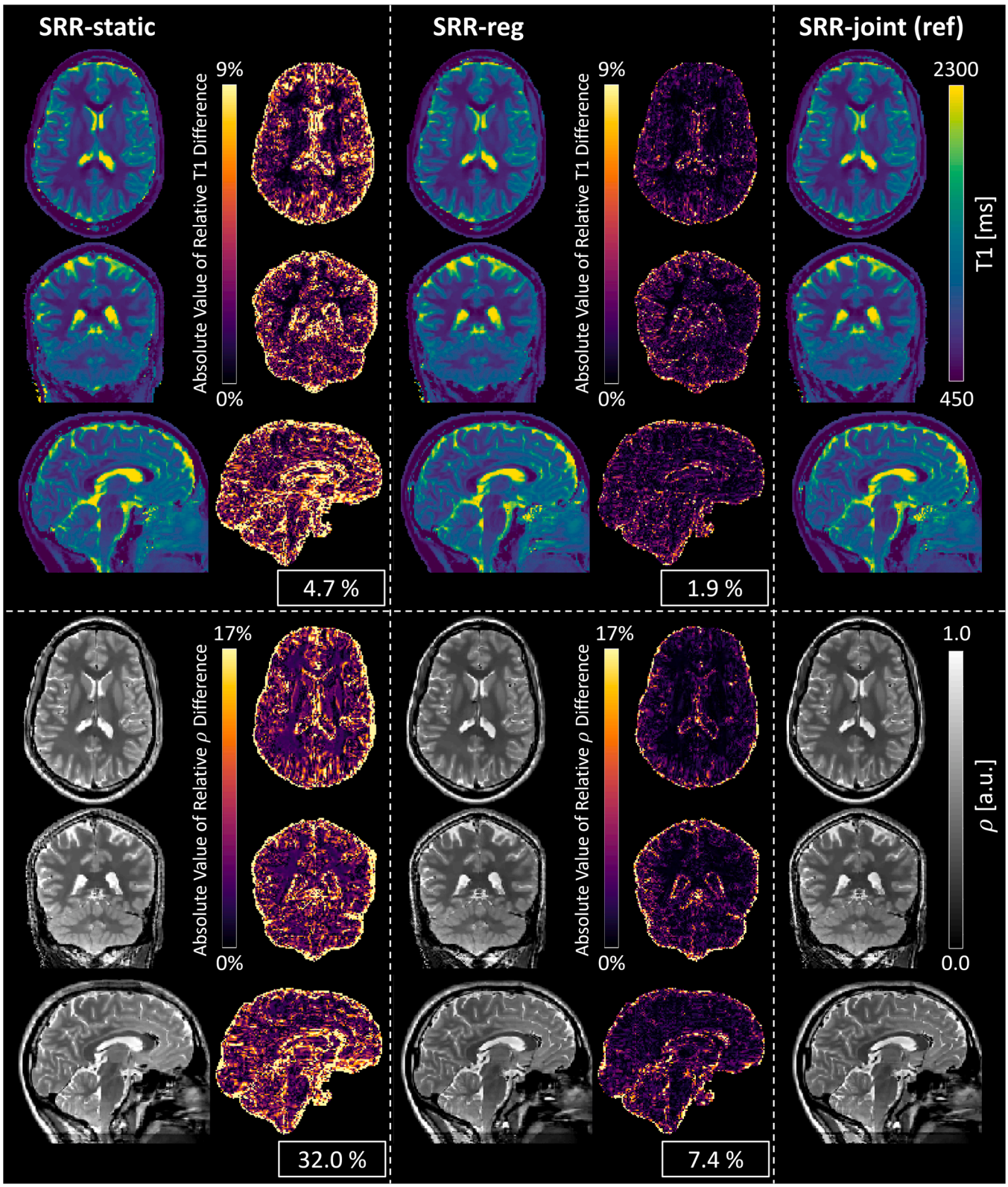

Fig. 4. Reconstruction results for the LR-T1w *in vivo* dataset showing orthogonal mid-slice views of the quantitative T_1 and ρ parameter maps obtained using SRR-static (left column), SRR-reg (middle column), and SRR-joint (right column), respectively. For comparison reasons, the absolute value of the relative difference maps for T_1 and ρ is shown, which is calculated using the SRR-joint reconstruction result as relative reference. Numbers in boxes represent the overall relative difference measure, which was obtained by calculating the spatial mean of the absolute value of the corresponding relative difference map.

Table 3
Quantitative performance measures for the *in vivo* T_1 mapping experiment, summarized for each SRR framework.

	SRR-static	SRR-reg	SRR-joint
Average edge width			
T_1 map [mm]	3.88	3.76	**3.67**
ρ map [mm]	2.92	2.50	**2.38**
SNR $_{VOI}$ in T_1 map			
white matter	97.1	99.6	**133.7**
CSF	30.1	32.4	**34.7**
caudate nucleus	35.2	38.6	**45.1**
SNR $_{VOI}$ in ρ map			
white matter	66.1	85.2	**93.6**
CSF	19.6	**22.8**	19.4
caudate nucleus	42.4	55.8	**59.9**

at the same TE, and the obtained T_2 and ρ parameter map estimates, respectively. From Fig. 6, it can be appreciated that SRR-joint enhances the spatial resolution, and reduces the partial volume effects present in the acquired MESE T_2-weighted images with low through-plane resolution. As a result, the interfaces and fine structural details of the different tissue types appear more clear in the quantitative T_2 and ρ parameter maps. Furthermore, to visually compare how the different SRR frameworks arrive at different parameter map estimates for the T_2-weighted dataset, Fig. 8 shows the absolute value of the relative difference between the reconstructed parameter maps obtained with SRR-static and SRR-reg, taking the parameter maps obtained with the SRR-joint framework as a reference.

In addition, Fig. 7 shows a directly acquired MESE T_2-weighted image with low through-plane resolution compared to synthesized T_2-weighted images with high through-plane resolution, that were produced from the SRR T_2 and ρ parameter map estimates for each framework. As can be appreciated from Fig. 7, SRR-joint outperforms SRR-static and SRR-reg, showing enhanced delineation of brain structures and a reduction in noise artifacts. We recall that identical regularization weights were used for the three SRR frameworks. Furthermore, it follows from Fig. 7 that the SRR-joint-T2w image shows improved detail in the axial view, which is the in-plane orientation of the LR image. This is probably due to reduced through-slice blurring.

Motion parameter estimates obtained using the SRR-reg and SRR-joint framework on the *in vivo* datasets are reported in Fig. 9. In particular, graphs of the translation and rotation parameters estimated for each LR image number are plotted. LR image numbers were ranked in order of acquisition. As indicated by the order of magnitude of the

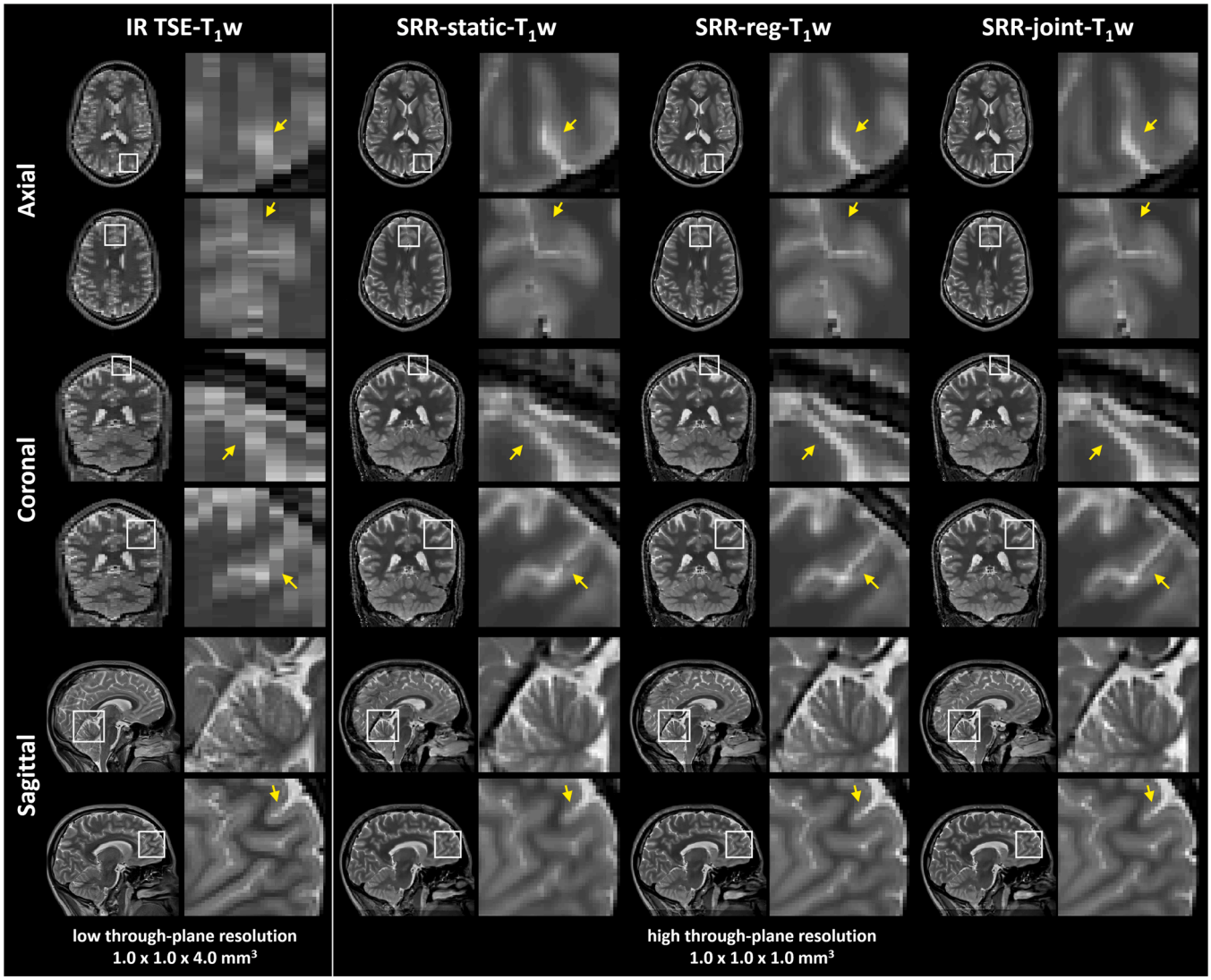

Fig. 5. Orthogonal mid-slice views with zoomed close-ups showing the resolution improvement for a directly acquired IR TSE T_1-weighted image with low through-plane resolution sampled at TI_1 (first column), compared to synthesized T_1-weighted images with high through-plane resolution (columns 2–4), that were produced from the SRR T_1 and ρ parameter map estimates for each framework, sampled at the same echo time.

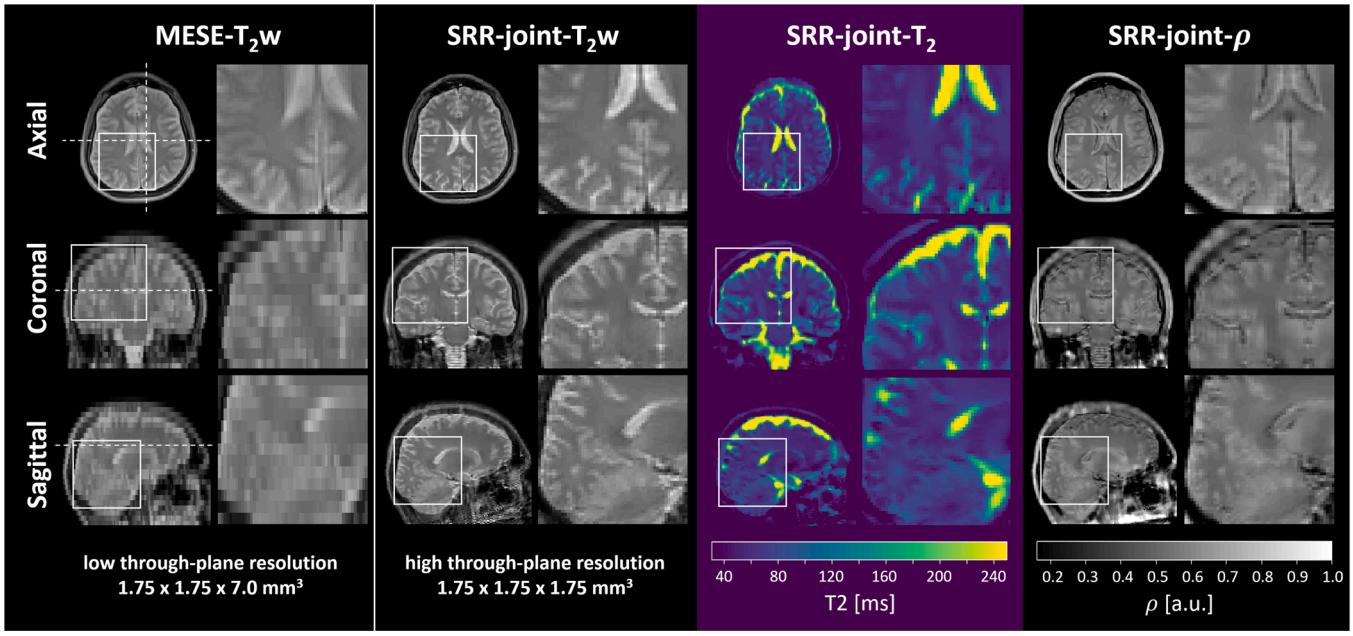

Fig. 6. Orthogonal mid-slice views with zoomed close-ups showing the resolution improvement for a directly acquired MESE T_2-weighted image with low through-plane resolution sampled at TE = 47.2 ms (first column), compared to a synthesized T_2-weighted image with high through-plane resolution (second column), that was produced from the SRR T_2 and ρ parameter map estimates (columns 3 and 4) sampled at the same echo time. Dashed lines indicate the slice locations.

estimated motion parameters, inter-image rigid motion was less present in the T_1-weighted dataset as compared to the T_2-weighted dataset. Although the motion parameter traces look very similar for SRR-joint and SRR-reg, small differences can still be observed that likely contribute to the superior performance of SRR-joint compared to SRR-reg.

Furthermore, by construction of the MESE sequence no inter-image motion should exist between the different LR images (*i.e.* different echoes) of the same MESE scan in the T_2-weighted dataset. Indeed, it follows from Fig. 9 that motion parameter estimates obtained using SRR-joint are consistent for the three LR image numbers corresponding with each MESE number. For SRR-reg, on the other hand, one can observe nonphysical differences of the motion parameter estimates for the LR image numbers per MESE number. This motion stability property can be further quantified by calculating the mean across MESE scans of the standard deviations across the echoes per individual MESE scan, for each motion parameter. Table 4 summarizes these values for SRR-reg and SRR-joint. As summarized in Table 4, SRR-joint arrives at significantly lower sample mean values compared to SRR-reg, indicating superior motion stability performance. Note that, both for SRR-joint and SRR-reg, a rigid motion parameter set was estimated per individual LR image.

Finally, to evaluate the convergence behavior of the three SRR methods in the *in vivo* T_1 and T_2 mapping experiments, Fig. 10 shows the cost function value and the 2-norm of the residual between the measured LR images and their predictions based on the estimated tissue and motion parameters as a function of the number of iterations. For both *in vivo*

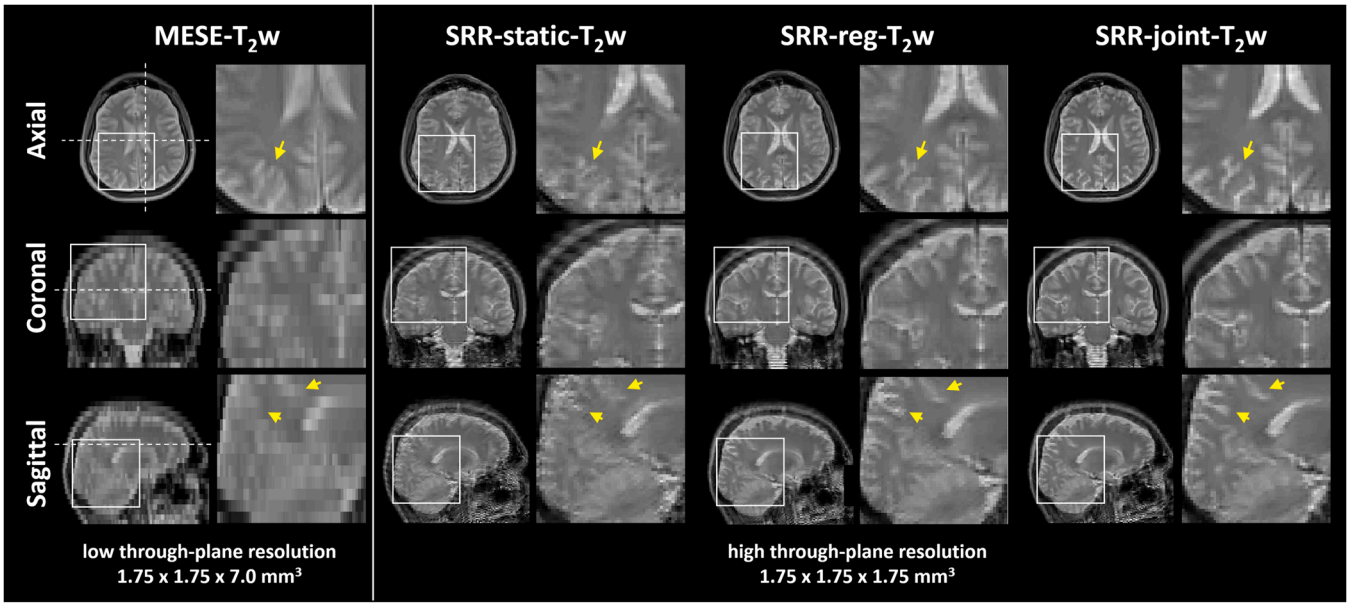

Fig. 7. Orthogonal mid-slice views with zoomed close-ups showing the resolution improvement for a directly acquired MESE T_2-weighted image with low through-plane resolution sampled at TE = 47.2 ms (first column), compared to synthesized T_2-weighted images with high through-plane resolution (columns 2–4), that were produced from the SRR T_2 and ρ parameter map estimates for each framework, sampled at the same echo time. Dashed lines indicate the slice locations.

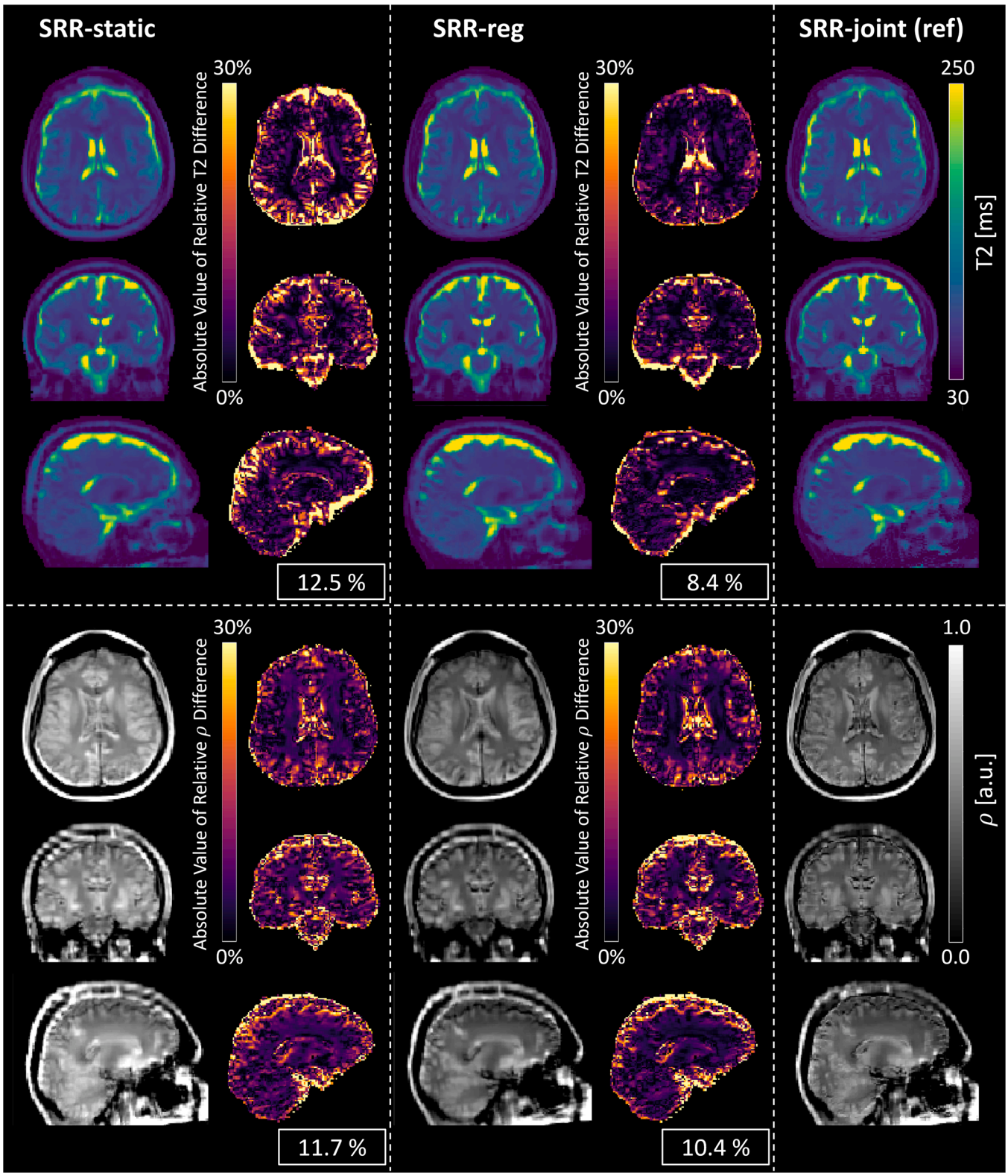

Fig. 8. Reconstruction results for the LR-T2w *in vivo* dataset showing orthogonal mid-slice views of the quantitative T_2 and ρ parameter maps obtained using SRR-static (left column), SRR-reg (middle column), and SRR-joint (right column), respectively. For comparison reasons, the absolute value of the relative difference maps for T_2 and ρ is shown, which is calculated using the SRR-joint reconstruction result as relative reference. Numbers in boxes represent the overall relative difference measure, which was obtained by calculating the spatial mean of the absolute value of the corresponding relative difference map.

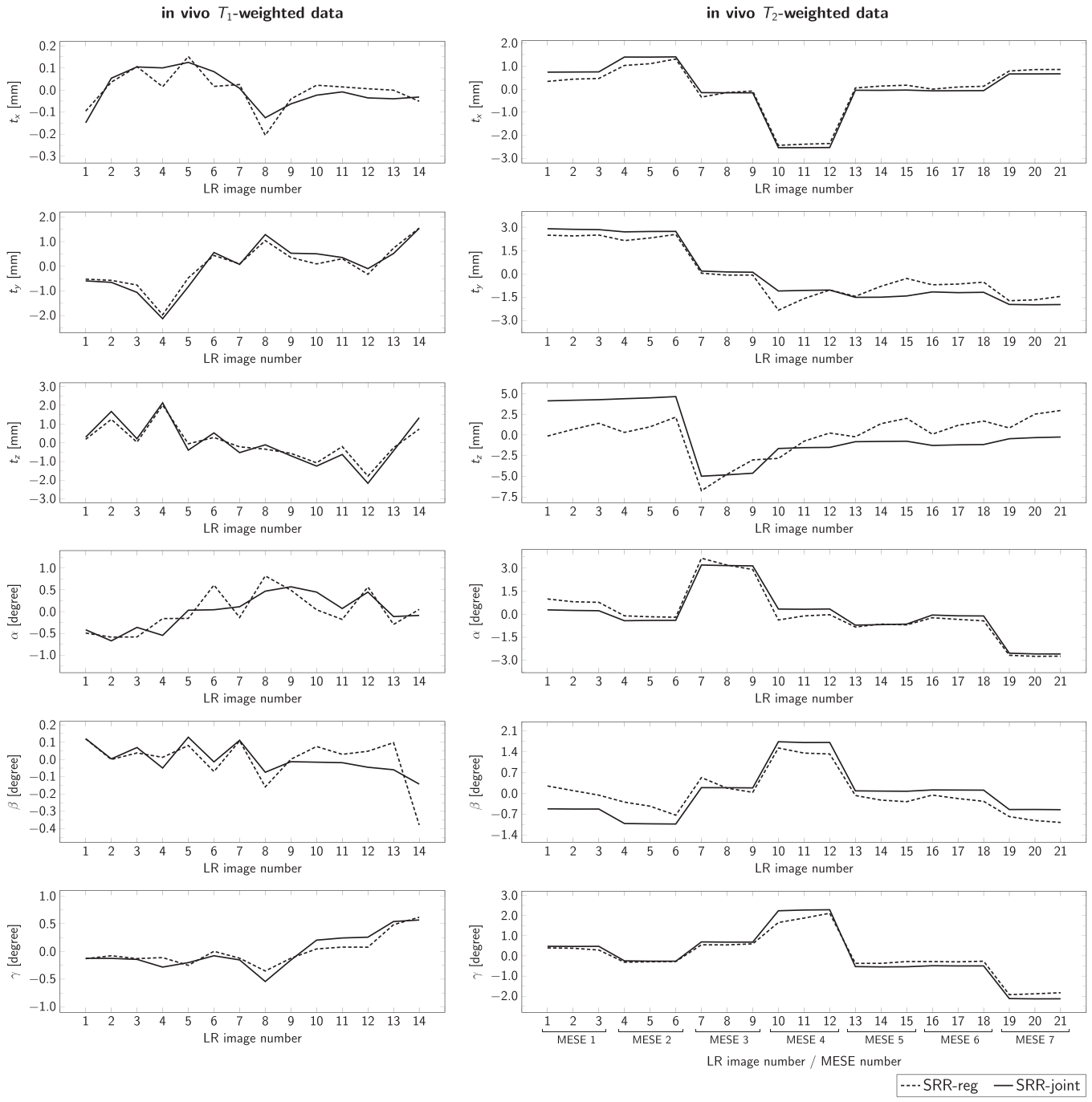

Fig. 9. Graphs of the motion parameter estimates that were obtained for the *in vivo* T_1-weighted dataset (left column) and T_2-weighted dataset (right column), using the SRR-reg and SRR-joint framework, respectively. The LR image numbers are ranked in order of acquisition. For the T_2-weighted dataset, the MESE numbers are indicated (right column, bottom graph) with their corresponding LR image numbers. Translation parameters are reported in millimeters, rotation parameters in degrees.

experiments, it can be observed that SRR-joint arrives at lower cost function values and lower residual values than SRR-static and SRR-reg.

5. Discussion

In this work, we presented a Bayesian framework for model-based motion-corrected SRR in qMRI. The framework allows the joint estimation of 3D isotropic HR tissue parameter maps and inter-image motion parameters from a set of multi-slice magnitude images with a low through-plane resolution. The framework's potential was demonstrated in both simulations and real data experiments, using T_1 and T_2 mapping as carrying examples. As follows from Table 2, the proposed SRR framework with joint motion estimation (SRR-joint) showed superior motion parameter estimation and, at the same time, improved tissue parameter mapping RMSE compared to previously published approaches without (SRR-static) and with (SRR-reg) motion pre-compensation. More specifically, the motion component RMMSE of SRR-joint was about an order of magnitude smaller compared to that of SRR-reg and even more for SRR-static. Furthermore, the overall relative RMSE of the tissue parameters T_1 and ρ for SRR-joint was about 20%

Table 4
Quantification of motion stability performance for the *in vivo* T_2-weighted data set. Tabulated values indicate the sample mean across the MESE scans of the standard deviations calculated across the echoes per individual MESE scan, for each motion parameter, using the SRR-reg and SRR-joint framework, respectively. Translation values are reported in millimeters, rotation values in degrees. Lower values indicate better performance.

	t_x [mm]	t_y [mm]	t_z [mm]	α [degree]	β [degree]	γ [degree]
SRR-reg	0.064	0.205	0.958	0.111	0.123	0.052
SRR-joint	0.004	0.023	0.075	0.020	0.005	0.007

smaller compared to that of SRR-reg and about 50% smaller compared to SRR-static. Finally, the proposed SRR-joint framework revealed sharper edges in the real data experiments, providing a noticeably better delineation of brain structures, as compared to SRR-reg and SRR-static.

Our proposed framework is modular with respect to the signal and noise model describing the MR data. That is, the T_1 or T_2 relaxation model used in this paper can easily be replaced by any other quantitative signal model. Examples may include SRR strategies for quantification T_2*-relaxation times of the knee (Smekens et al., 2021), blood flow in single post labeling delay pseudo-Continuous Arterial Spin Labeling (Bladt et al., 2020), or diffusion (Van Steenkiste et al., 2016). In addition, the framework is modular with respect to the assumed distribution of the MR data. Indeed, MR data can be characterized by various noise distributions (other than the Rice distribution), considering either single-coil or multi-coil acquisition systems (den Dekker and Sijbers, 2014). Examples include the noncentral chi distribution, which is valid for magnitude images reconstructed from multi-coil data using the sum-of-squares method (Constantinides et al., 1997), or data distributions that occur for parallel MRI techniques which perform undersampling of the *k*-space to reduce the acquisition time, such as SENSE or GRAPPA (Aja-Fernández et al. 2016). Our Bayesian joint motion and tissue parameter estimation framework can be easily adapted towards any of these data distributions.

Unlike various SRR methods in the literature that rely on orthogonal slice orientations, our method allows for arbitrary slice orientations, which offers much more flexibility with respect to sampling of the *k*-space and setting the contrast weightings. This increased *k*, *q*-space sampling flexibility is a key asset for optimal experiment design studies aimed at the estimation of quantitative tissue parameters with the highest precision (Poot et al., 2010a; Zhao et al., 2019). In future work, we intend to investigate, given a fixed acquisition time and relying on Cramér-Rao lower bound analysis, the best slice direction and contrast weighting combination of each of the LR images in terms of the precision with which qMRI parameters can be estimated with our proposed SRR-joint framework. Preliminary results of this study for SRR-static have recently been reported by Nicastro *et al.* (Nicastro et al., 2020).

The current framework has some limitations. First, while the framework corrects for motion between the LR multislice images, intra- and inter-slice motion is not yet accounted for. To compensate for intra-slice motion, our framework could be combined with prospective motion correction strategies (Gao et al., 2021; Maclaren et al., 2013). Furthermore, inter-slice motion could be accounted for by adding motion parameters for each individual slice of the LR images and estimating these parameters jointly with the HR tissue parameter maps. Note, however, that although such an approach may improve the accuracy of the estimated maps, the addition of extra parameters to be estimated comes at the expense of a reduced precision. Hence, both effects should be carefully weighed against each other. The extension of our framework to include inter-slice motion and the trade-off between accuracy and precision that comes with it are subject of future investigation.

Second, in this work the hyperparameters of the prior distributions (9) are selected by casting the Bayesian MAP estimation problem as a regularized optimization problem of which the regularization weights are chosen empirically, aiming at equal contributions of the different

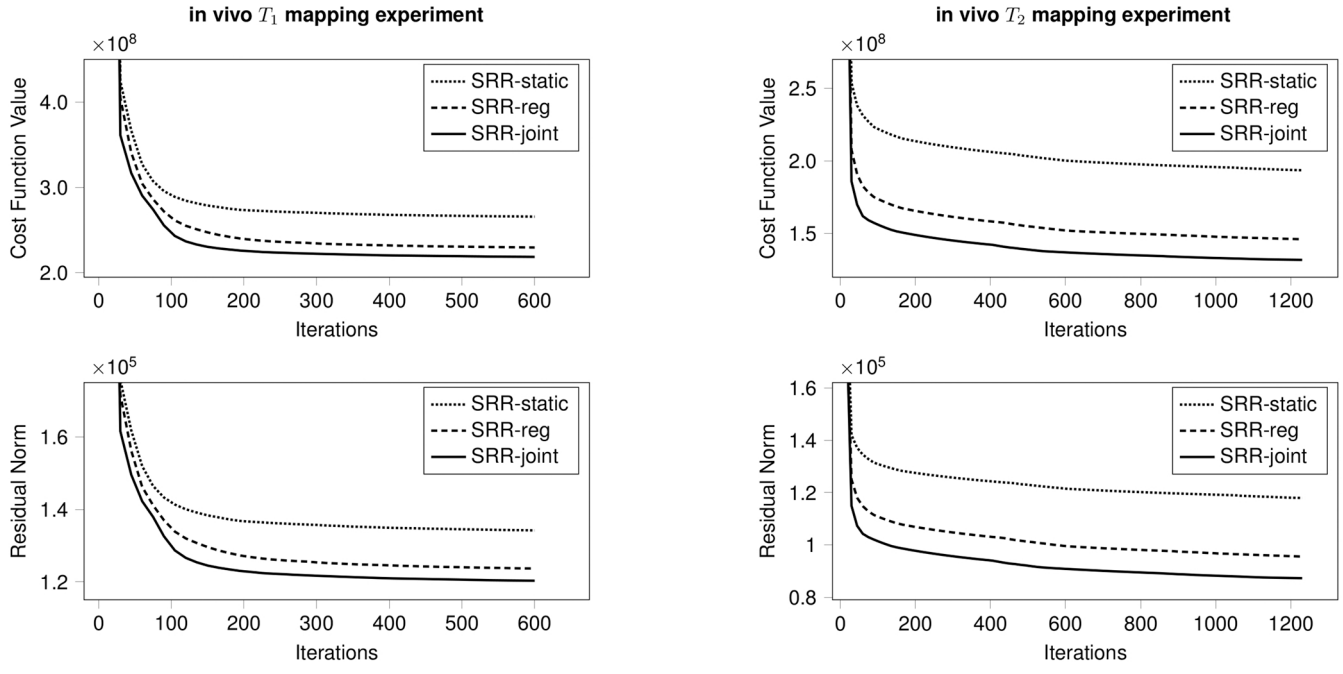

Fig. 10. Convergence plots showing the cost function value and the residual norm as function of the iterations for the *in vivo* T_1 mapping experiment (left column) and T_2 mapping experiment (right column), respectively.

regularization terms. This approach may be sub-optimal. To the best of our knowledge, however, there is no consensus on the optimal selection strategy of regularization parameters in a multi-parameter nonlinear regression problem like the one at hand. Nevertheless, we hypothesize that choosing the (hyperparameters of the) prior distributions based on prior acquisitions or learning them from available (q)MRI databases may be promising alternative approaches, which are subject of ongoing research.

Finally, the existence of fast 2D multi-slice protocols for MR relaxometry parameter mapping is crucial to fully exploit the benefits of model-based SRR, and to allow for clinically acceptable scan times. The proof-of-concept acquisitions in this paper aim to illustrate the advantages of joint motion estimation. The combination of model-based SRR with state-of-the-art sequences applying undersampling strategies to further reduce acquisition time is subject of future work. As an example, recent work for T_2 mapping discussed the use of GRAPPATINI (Hilbert et al., 2018), a fast prototype sequence allowing for block-based Cartesian undersampling of *k*-space combined with additional GRAPPA acceleration. Its potential for model-based SRR has been previously reported (Bano et al., 2020), albeit without any appropriate motion estimation routine for SRR. We are convinced that our work can serve as an extension to such an approach and to other model-based SRR frameworks that only account for motion using pre-compensation routines.

6. Conclusion

In conventional model-based SRR approaches for qMRI, it is common practice to compensate for motion prior to the SRR, *e.g.* by using a pre-registration routine. However, as demonstrated in this paper, this conventional two-step approach lacks high accuracy motion estimation and leads to biased parameter estimates. Hence, we have proposed a rigorous unified framework for model-based SRR with joint motion estimation using a Bayesian Maximum A Posteriori (MAP) estimator. The framework allows the joint estimation of 3D isotropic HR tissue parameter maps and inter-image motion parameters from a set of multi-slice magnitude images with a low through-plane resolution. Our SRR framework, which is modular with respect to the quantitative signal model and the assumed distribution of the MR data, has been validated in synthetic whole brain simulations and also with two *in vivo* human brain data sets, for T_1 and T_2 mapping, respectively. It has been demonstrated that the proposed SRR framework provides a more detailed delineation of brain structures and shows superior motion parameter estimation and improved tissue parameter mapping RMSE compared to state-of-the-art SRR approaches.

CRediT authorship contribution statement

Quinten Beirinckx: Conceptualization, Methodology, Software, Validation, Formal analysis, Investigation, Writing – original draft, Writing – review & editing, Visualization. **Ben Jeurissen:** Methodology, Software, Writing – review & editing. **Michele Nicastro:** Methodology, Software, Investigation, Writing – review & editing. **Dirk H. J. Poot:** Methodology, Writing – review & editing. **Marleen Verhoye:** Resources, Writing – review & editing, Funding acquisition. **Arnold J. den Dekker:** Conceptualization, Methodology, Formal analysis, Writing – review & editing, Supervision, Funding acquisition. **Jan Sijbers:** Conceptualization, Methodology, Resources, Writing – review & editing, Supervision, Funding acquisition.

Declaration of competing interest

The authors declare that they have no known competing financial interests or personal relationships that could have appeared to influence the work reported in this paper.

Acknowledgments

The authors gratefully acknowledge support from Belgian Science Policy Prodex (Grant ISLRA 2009–1062), and the Research Foundation Flanders, Belgium (FWO) through project funding G084217N and 12M3119N. In addition, this project has received funding from the European Union's Horizon 2020 research and innovation program under the Marie Skłodowska-Curie grant agreement No 764513. Finally, the authors would like to thank Floris Vanhevel and Céline Smekens for their help during the acquisition of the *in-vivo* datasets and Prof. Dr. P.M. Parizel for his kind support in the initial phase of the project.

Supplementary materials

Supplementary material associated with this article can be found in the online version at doi:10.1016/j.compmedimag.2022.102071.

References

Aja-Fernández, S., Vegas-Sánchez-Ferrero, G., Tristán-Vega, A., 2014. Noise estimation in parallel MRI: GRAPPA and SENSE. Magn. Reson. Imaging 32, 281–290. https://doi.org/10.1016/j.mri.2013.12.001.

Aja-Fernández, S., Pieciak, T., Sánchez-Ferrero, G.V., 2015. Spatially variant noise estimation in MRI: a homomorphic approach. Med. Image Anal. 20, 184–197. https://doi.org/10.1016/j.media.2014.11.005.

Aja-Fernández, S., Pieciak, T., Sánchez-Ferrero, G.V., 2016. Statistical Analysis of Noise in MRI: Modeling, Filtering and Estimation, 1ed.,. Springer International Publishing, Cham, Switzerland. https://doi.org/10.1007/978-3-319-39934-8.

Bano, W., Piredda, G.F., Davies, M., Marshall, I., Golbabaee, M., Meuli, R., Kober, T., Thiran, J.P., Hilbert, T., 2020. Model-based super-resolution reconstruction of T2 maps. Magn. Reson. Med. 83, 906–919. https://doi.org/10.1002/mrm.27981.

Barral, J.K., Gudmundson, E., Stikov, N., Etezadi-Amoli, M., Stoica, P., Nishimura, D.G., 2010. A robust methodology for in vivo T1 mapping. Magn. Reson. Med. 64, 1057–1067. https://doi.org/10.1002/mrm.22497.

Beck, A., Tetruashvili, L., 2013. On the convergence of block coordinate descent type methods. SIAM J. Optim. 23, 2037–2060. https://doi.org/10.1137/120887679.

Beirinckx, Q., Ramos-Llordén, G., Jeurissen, B., Poot, D.H.J., Parizel, P.M., Verhoye, M., Sijbers, J., den Dekker, A.J., 2020. Joint maximum likelihood estimation of motion and T1 parameters from magnetic resonance images in a super-resolution framework: a simulation study. Fundam. Inform. 172, 105–128. https://doi.org/10.3233/FI-2020-1896.

Bladt, P., Beirinckx, Q., van der Plas, M.C.E., Schmid, S., Teeuwisse, W.M., Jeurissen, B., den Dekker, A.J., Sijbers, J., van Osch, M.J.P., 2020. Super-resolution reconstruction of single-PLD pseudo-continuous ASL images. Proc. Int. Soc. Mag. Reson. Med 28, 3293.

van den Bos, A., 2007. Parameter Estimation for Scientists and Engineers. John Wiley & Sons, Hoboken, New Yersey, USA. https://doi.org/10.1002/9780470173862.

Bouhrara, M., Bonny, J.M., Ashinsky, B.G., Maring, M.C., Spencer, R.G., 2017. Noise estimation and reduction in magnetic resonance imaging using a new multispectral nonlocal maximum-likelihood filter. IEEE Trans. Med. Imag. 36, 181–193. https://doi.org/10.1109/TMI.2016.2601243.

Carr, H.Y., Purcell, E.M., 1954. Effects of diffusion on free precession in nuclear magnetic resonance experiments. Phys. Rev. 94, 630–638. https://doi.org/10.1103/PhysRev.94.630.

Chambolle, A., Levine, S.E., Lucier, B.J., 2011. An upwind finite-difference method for total variation-based image smoothing. SIAM J. Imaging Sci. 4, 277–299. https://doi.org/10.1137/090752754.

Christiaens, D., Cordero-Grande, L., Pietsch, M., Hutter, J., Price, A.N., Hughes, E.J., Vecchiato, K., Deprez, M., Edwards, A.D., Hajnal, J.V., Tournier, J.D., 2021. Scattered slice SHARD reconstruction for motion correction in multi-shell diffusion MRI. NeuroImage 225, 117437. https://doi.org/10.1016/j.neuroimage.2020.117437.

Coleman, T.F., Li, Y., 1994. On the convergence of reflective Newton methods for large-scale minimization subject to bounds. Math. Program. 67, 189–224. https://doi.org/10.1007/BF01582221.

Constantinides, C.D., Atalar, E., McVeigh, E.R., 1997. Signal-to-noise measurements in magnitude images from NMR phased arrays. Magn. Reson. Med. 38, 852–857. https://doi.org/10.1002/mrm.1910380524.

Coupé, P., Manjón, J.V., Gedamu, E., Arnold, D., Robles, M., Collins, D.L., 2010. Robust Rician noise estimation for MR images. Med. Image Anal. 14, 483–493. https://doi.org/10.1016/j.media.2010.03.001.

den Dekker, A.J., Sijbers, J., 2014. Data distributions in magnetic resonance images: a review. Phys. Med 30, 725–741. https://doi.org/10.1016/j.ejmp.2014.05.002.

Ebner, M., Wang, G., Li, W., Aertsen, M., Patel, P.A., Aughwane, R., Melbourne, A., Doel, T., Dymarkowski, S., De Coppi, P., David, A.L., Deprest, J., Ourselin, S., Vercauteren, T., 2020. An automated framework for localization, segmentation and super-resolution reconstruction of fetal brain MRI. NeuroImage 206, 116324. https://doi.org/10.1016/j.neuroimage.2019.116324.

Fessler, J.A., Kim, D., 2011. Axial block coordinate descent (ABCD) algorithm for X-ray CT image reconstruction. Proc. Int. Mtg. Full. 3D Image Recon. Rad. Nuc. Med 262–265.

Fogtmann, M., Seshamani, S., Kim, K., Chapman, T., Studholme, C., 2012. A unified approach for motion estimation and super resolution reconstruction from structural Magnetic Resonance imaging on moving subjects. MICCAI Workshop Perinat. Paediatr. Imag. 9–26.

Fogtmann, M., Seshamani, S., Kroenke, C., Cheng, X., Chapman, T., Wilm, J., Rousseau, F., Studholme, C., 2014. A unified approach to diffusion direction sensitive slice registration and 3-D DTI reconstruction from moving fetal brain anatomy. IEEE Trans. Med. Imag. 33, 272–289. https://doi.org/10.1109/tmi.2013.2284014.

Gao, X., Hucker, P., Hennig, J., Zaitsev, M., 2021. Strategies to improve intratrain prospective motion correction for turbo spin-echo sequences with constant flip angles. Magn. Reson. Med. 86, 852–865. https://doi.org/10.1002/mrm.28763.

Gholipour, A., Estroff, J.A., Warfield, S.K., 2010. Robust super-resolution volume reconstruction from slice acquisitions: application to fetal brain MRI. IEEE Trans. Med. Imag. 29, 1739–1758. https://doi.org/10.1109/tmi.2010.2051680.

Greenspan, H., Oz, G., Kiryati, N., Peled, S., 2002. MRI inter-slice reconstruction using super-resolution. Magn. Reson. Imaging 20, 437–446. https://doi.org/10.1016/s0730-725x(02)00511-8.

Hilbert, T., et al., 2018. Accelerated T2 mapping combining parallel MRI and model-based reconstruction: GRAPPATINI. J. Magn. Reson. Imaging 48, 359–368. https://doi.org/10.1002/jmri.25972.

Jiang, S., Xue, H., Glover, A., Rutherford, M., Rueckert, D., Hajnal, J.V., 2007. MRI of moving subjects using multislice snapshot images with volume reconstruction (SVR): application to fetal. Neonatal, Adult Brain Stud. IEEE Trans. Med. Imag. 26, 967–980. https://doi.org/10.1109/TMI.2007.895456.

Kainz, B., Steinberger, M., Wein, W., Kuklisova-Murgasova, M., Malamateniou, C., Keraudren, K., Torsney-Weir, T., Rutherford, M., Aljabar, P., Hajnal, J.V., Rueckert, D., 2015. Fast volume reconstruction from motion corrupted stacks of 2D slices. IEEE Trans. Med. Imag. 34, 1901–1913. https://doi.org/10.1109/TMI.2015.2415453.

Lajous, H., Hilbert, T., Roy, C.W., Tourbier, S., de Dumast, P., Yu, T., Thiran, J.P., J.-B, L., Piccini, D., Hagmann, P., Meuli, R., Kober, T., Stuber, M., van Heeswijk, R.B., Bach Cuadraet, M., 2020. T2 mapping from super-resolution-reconstructed clinical fast spin echo magnetic resonance acquisitions. In: Martel, A.L., et al. (Eds.), Medical Image Computing and Computer-Assisted Intervention - MICCAI, 2020. Springer, Cham, pp. 114–124. https://doi.org/10.1007/978-3-030-59713-9_12.

Maclaren, J., Herbst, M., Speck, O., Zaitsev, M., 2013. Prospective motion correction in brain imaging: a review. Magn. Reson. Med. 69, 621–636. https://doi.org/10.1002/mrm.24314.

Maier, O., Schoormans, J., Schloegl, M., Strijkers, G.J., Lesch, A., Benkert, T., Block, T., Coolen, B.F., Bredies, K., Stollberger, R., 2019. Rapid T1 quantification from high resolution 3D data with model-based reconstruction. Magn. Reson. Med. 81, 2072–2089. https://doi.org/10.1002/mrm.27502.

Maitra, R., Faden, D., 2009. Noise estimation in magnitude MR datasets. IEEE Trans. Med. Imag. 28, 1615–1622. https://doi.org/10.1109/TMI.2009.2024415.

de Mello, R., Ma, Y., Ji, Y., Du, J., Chang, E.Y., 2019. Quantitative MRI musculoskeletal techniques: an update. AJR Am. J. Roentgenol. 213, 524–533. https://doi.org/10.2214/AJR.19.21143.

Nachmani, A., Schurr, R., Joskowicz, L., Mezer, A.A., 2019. The effect of motion correction interpolation on quantitative T1 mapping with MRI. Med. Image Anal. 52, 119–127. https://doi.org/10.1016/j.media.2018.11.012.

Nicastro, M., Beirinckx, Q., Bladt, P., Jeurissen, B., Klein, S., Sijbers, J., Poot, D.H.J., den Dekker, A.J., 2020. Optimal design of a T_1 super-resolution reconstruction experiment: a simulation study. Abstr. Book 12th Annu. Meet. ISMRM Benelux Chapter pp. P-008.

Petrovic, A., Scheurer, E., Stollberger, R., 2015. Closed-form solution for T2 mapping with nonideal refocusing of slice selective CPMG sequences. Magn. Reson. Med. 73, 818–827. https://doi.org/10.1002/mrm.25170.

Pieciak, T., Aja-Fernández, S., Sánchez-Ferrero, G.V., 2017. Non-stationary Rician noise estimation in parallel MRI using a single image: a variance-stabilizing approach. IEEE Trans. Pattern Anal. Mach. Intell. 39, 2015–2029. https://doi.org/10.1109/TPAMI.2016.2625789.

Plenge, E., Poot, D.H.J., Bernsen, M., Kotek, G., Houston, G., Wielopolski, P., van der Weerd, L., Niessen, W.J., Meijering, E., 2012. Super-resolution methods in MRI: can they improve the trade-off between resolution, signal-to-noise ratio, and acquisition time? Magn. Reson. Med. 68, 1983–1993. https://doi.org/10.1002/mrm.24187.

Poot, D.H.J., denDekker, A.J., Achten, E., Verhoye, M., Sijbers, J., 2010a. Optimal experimental design for diffusion kurtosis imaging. IEEE Trans. Med. Imag. 29, 819–829. https://doi.org/10.1109/TMI.2009.2037915.

Poot, D.H.J., Van Meir, V., Sijbers, J., 2010b. General and efficient super-resolution method for multi-slice MRI. Med. Image Comput. Comput. -Assist. Interv. -MICCAI 2010, 615–622. https://doi.org/10.1007/978-3-642-15705-9_75.

Poot, D.H.J., Jeurissen, B., Bastiaensen, Y., Veraart, J., Van Hecke, W., Parizel, P.M., Sijbers, J., 2013. Super-resolution for multislice diffusion tensor imaging. Magn. Reson. Med. 69, 103–113. https://doi.org/10.1002/mrm.24233.

Ramos-Llordén, G., den Dekker, A.J., Van Steenkiste, G., Jeurissen, B., Vanhevel, F., Van Audekerke, J., Verhoye, M., Sijbers, J., 2017. A unified maximum likelihood framework for simultaneous motion and T_1 estimation in quantitative MR T_1 mapping. IEEE Trans. Med. Imag. 36, 433–446. https://doi.org/10.1109/TMI.2016.2611653.

Rousseau, F., Glenn, O., Iordanova, B., Rodriguez-Carranza, C., Vigneron, D., Barkovich, J., Studholme, C., 2006. Registration-based approach for reconstruction of high-resolution in utero fetal MR brain images. Acad. Radiol. 13, 1072–1081. https://doi.org/10.1016/j.acra.2006.05.003.

Rousseau, F., Kim, K., Studholme, C., Koob, M., Dietemann, J.L., 2010. On super-resolution for fetal brain MRI. Med. Image Comput. Comput. -Assist. Interv. -MICCAI 2010, PT II 355–362.

Scherrer, B., Gholipour, A., Warfield, S.K., 2012. Super-resolution reconstruction to increase the spatial resolution of diffusion weighted images from orthogonal anisotropic acquisitions. Med. Image Anal. 16, 1465–1476. https://doi.org/10.1016/j.media.2012.05.003.

Seiler, A., Nöth, U., Hok, P., Reiländer, A., Maiworm, M., Baudrexel, S., Meuth, S., Rosenow, F., Steinmetz, H., Wagner, M., Hattingen, E., Deichmann, R., Gracien, R. M., 2021. Multiparametric quantitative MRI in neurological diseases. Front. Neurol. 12, 287. https://doi.org/10.3389/fneur.2021.640239.

Shilling, R.Z., Robbie, T.Q., Bailloeul, T., Mewes, K., Mersereau, R.M., Brummer, M.E., 2009. A super-resolution framework for 3-D high-resolution and high-contrast imaging using 2-D multislice MRI. IEEE Trans. Med. Imag. 28, 633–644. https://doi.org/10.1109/TMI.2008.2007348.

Sijbers, J., den Dekker, A.J., Scheunders, P., Van Dyck, D., 1998. Maximum-likelihood estimation of Rician distribution parameters. IEEE Trans. Med. Imag. 17, 357–361. https://doi.org/10.1109/42.712125.

Smekens, C., Beirinckx, Q., Vanhevel, F., Van Dyck, P., den Dekker, A.J., Sijbers, J., Janssens, T., Jeurissen, B., 2021. Super-resolution T2* mapping of the knee using UTE Spiral VIBE MRI. Proc. Int. Soc. Mag. Reson. Med 3920.

Smith, S.M., 2002. Fast robust automated brain extraction. Hum. Brain Mapp. 17, 143–155. https://doi.org/10.1002/hbm.10062.

Sui, Y., Afacan, O., Gholipour, A., Warfield, S.K., 2021. Fast and high-resolution neonatal brain MRI through super-resolution reconstruction from acquisitions with variable slice selection direction. Front. Neurosci. 15, 709. https://doi.org/10.3389/fnins.2021.636268.

van Houdt, P.J., Yang, Y., van der Heide, U.A., 2021. Quantitative magnetic resonance imaging for biological image-guided adaptive radiotherapy. Front. Oncol. 10, 3190. https://doi.org/10.3389/fonc.2020.615643.

Van Reeth, E., Tham, I.W., Tan, C.H., Poh, C.L., 2012. Super-resolution in magnetic resonance imaging: a review. Concepts Magn. Reson 40A, 306–325. https://doi.org/10.1002/cmr.a.21249.

Van Steenkiste, G., Jeurissen, B., Veraart, J., den Dekker, A.J., Parizel, P.M., Poot, D.H.J., Sijbers, J., 2016. Super-resolution reconstruction of diffusion parameters from diffusion-weighted images with different slice orientations. Magn. Reson. Med. 75, 181–195. https://doi.org/10.1002/mrm.25597.

Van Steenkiste, G., Poot, D.H.J., Jeurissen, B., den Dekker, A.J., Vanhevel, F., Parizel, P. M., Sijbers, J., 2017. Super-resolution T1 estimation: quantitative high resolution T1 mapping from a set of low resolution T1-weighted images with different slice orientations. Magn. Reson. Med. 77, 1818–1830. https://doi.org/10.1002/mrm.26262.

Walsh, D.O., Gmitro, A.F., Marcellin, M.W., 2000. Adaptive reconstruction of phased array MR imagery. Magn. Reson. Med 43, 682–690, 10.1002/(SICI)1522-2594(200005)43:53.0.CO;2-G.

Zhang, T., Pauly, J.M., Levesque, I.R., 2015. Accelerating parameter mapping with a locally low rank constraint. Magn. Reson. Med. 73, 655–661. https://doi.org/10.1002/mrm.25161.

Zhao, B., Haldar, J.P., Christodoulou, A.G., Liang, Z., 2012. Image reconstruction from highly undersampled (k, t)-space data with joint partial separability and sparsity constraints. IEEE Trans. Med. Imag. 31, 1809–1820. https://doi.org/10.1109/TMI.2012.2203921.

Zhao, B., Haldar, J.P., Liao, C., Ma, D., Jiang, Y., Griswold, M.A., Setsompop, K., Wald, L. L., 2019. Optimal experiment design for magnetic resonance fingerprinting: cramér-rao bound meets spin dynamics. IEEE Trans. Med. Imag. 38, 844–861. https://doi.org/10.1109/TMI.2018.2873704.